JAMES | Journal of Advances in Modeling Earth Systems®

RESEARCH ARTICLE
10.1029/2024MS004453

Multiscale Modeling Framework Using Element-Based Galerkin Methods for Moist Atmospheric Limited-Area Simulations

Soonpil Kang[1,2], James F. Kelly[3], Anthony P. Austin[1], and Francis X. Giraldo[1]

[1]Department of Applied Mathematics, Naval Postgraduate School, Monterey, CA, USA, [2]Atmospheric, Earth, and Energy Division, Lawrence Livermore National Laboratory, Livermore, CA, USA, [3]Space Science Division, U.S. Naval Research Laboratory, Washington, DC, USA

Key Points:

- A multiscale modeling framework (MMF) for moist atmospheric limited-area simulations is developed
- The large-scale and small-scale processes in the framework are modeled using a nonhydrostatic model and an element-based Galerkin method
- The MMF improves the representation of moist dynamics for cloud processes

Correspondence to:
S. Kang,
kang18@llnl.gov

Citation:
Kang, S., Kelly, J. F., Austin, A. P., & Giraldo, F. X. (2025). Multiscale modeling framework using element-based Galerkin methods for moist atmospheric limited-area simulations. *Journal of Advances in Modeling Earth Systems*, *17*, e2024MS004453. https://doi.org/10.1029/2024MS004453

Received 16 MAY 2024
Accepted 15 JUN 2025

Author Contributions:
Conceptualization: Francis X. Giraldo
Funding acquisition: James F. Kelly, Anthony P. Austin, Francis X. Giraldo
Investigation: Soonpil Kang, James F. Kelly
Methodology: Soonpil Kang, James F. Kelly, Francis X. Giraldo
Project administration: Francis X. Giraldo
Resources: Francis X. Giraldo
Software: Soonpil Kang
Supervision: Francis X. Giraldo
Validation: Soonpil Kang, James F. Kelly, Anthony P. Austin, Francis X. Giraldo
Visualization: Soonpil Kang
Writing – original draft: Soonpil Kang

Abstract This paper presents a multiscale modeling framework (MMF) to model moist atmospheric limited-area weather. The MMF resolves large-scale convection using a coarse grid while simultaneously resolving local features through numerous fine local grids and coupling them seamlessly. Both large- and small-scale processes are modeled using the compressible Navier-Stokes equations within the Nonhydrostatic Unified Model of the Atmosphere (NUMA), and are discretized using a continuous element-based Galerkin method (spectral elements) with high-order basis functions. Consequently, the large-scale and small-scale models share the same dynamical core but have the flexibility to be adjusted individually. The proposed MMF method is tested in 2D and 3D idealized limited-area weather problems involving storm clouds produced by squall line and supercell simulations. Numerical results from the MMF showed enhanced representation of cloud processes compared to the coarse model.

Plain Language Summary Conventional Numerical Weather Prediction (NWP) models represent convective processes using a subgrid-scale parameterization. The large-scale convective processes typically use grids with relatively low resolution, while resolving small-scale cloud processes requires much higher resolution. To efficiently address this multiscale problem, the multiscale modeling framework (MMF) simulates the large-scale process on a lower resolution grid, while incorporating multiple, independent higher resolution grids to simulate local cloud processes. We present an MMF in which the large-scale and small-scale models are constructed using similar mathematical models and high-order discretization methods.

1. Introduction

Atmospheric flows, within the context of weather and climate, encompass a wide spectrum of spatial and temporal scales. These scales range from thousands of kilometers for general circulation to hundreds of meters for precipitation microphysics. The multiscale nature of these phenomena poses a significant computational challenge for accurately simulating the atmosphere. To address this challenge, deep moist convection can be represented by conventional subgrid-scale parameterizations or by simulating them explicitly. General circulation models (GCMs) for the moist atmosphere typically resolve the large-scale process (LSP), while parameterizing unresolved information from the small-scale processes (SSPs). Conventional parameterizations contain modeling approximations that are difficult to quantify and consequently require significant efforts for tuning free parameters. For an operational weather model, the calibration process needs to be performed for each numerical setup and different suite of parameterizations. In contrast, the multiscale modeling framework (MMF) aims to explicitly resolve both the LSP and SSP on different grids and couples them through their interaction—an advantage of this approach is that the separation of scales resolved by both models is clearly defined. The LSP represents the general convective process, while the SSP represents the cloud-scale process. Within this framework, the LSP model forces the SSP model and receives feedback from it. Since the SSP model is based on the dynamics equations, the modeling bias is minimized, unlike traditional parameterizations.

MMF methods have been proposed for weather and climate simulations to replace traditional semi-empirical parameterizations used by cloud-resolving models (CRMs). Grabowski and Smolarkiewicz (Grabowski & Smolarkiewicz, 1999) proposed a computational framework termed cloud resolving convection parameterization (CRCP) and later referred to it as superparameterization (Grabowski, 2004). This framework is designed to capture explicitly both large-scale and cloud-scale dynamics and couple them through relaxation and has been

Writing – review & editing:
Soonpil Kang, James F. Kelly, Anthony P. Austin, Francis X. Giraldo

shown to improve the representation of small- and mesoscale processes. Randall et al. (2003) provide a comprehensive summary of the initial ideas behind superparameterization, which offers a promising alternative to conventional parameterizations in precipitation simulations, despite its high computational cost. Khairoutdinov and Randall (M. F. Khairoutdinov & Randall, 2001; M. Khairoutdinov et al., 2005) developed a superparameterized version of the NCAR Community Atmosphere Model (SP-CAM). It was shown that SP-CAM improves the variability of precipitation over the land and ocean, closely matching the observed precipitation frequency. Recent investigations on the performance of SP-CAM variants with a particular focus on rain statistics are available in the literature (Kooperman et al., 2016). This improvement of MMF over conventional parameterizations for representing precipitation was also demonstrated in Pritchard & Somerville (2009). The Department of Energy Superparameterized Energy Exascale Earth System Model (SP-E3SM) (Hannah et al., 2020; Lin et al., 2022) combines a spectral-element based dynamical core with the System for Atmospheric Modeling (SAM) (M. F. Khairoutdinov & Randall, 2003) as a CRM. SP-E3SM produces more accurate mesoscale convective systems and realistic tropical waves compared to its standard version. This work has recently been extended to incorporate land surface processes, such as soil moisture, into their CRM (Lin et al., 2023), which is crucial for global climate modeling. Majda and Grooms (Majda & Grooms, 2014) presented a formulation of stochastic superparameterization wherein an eddy closure is derived from the stochastic modeling of the SSPs. The effectiveness of this formulation is examined on idealized mathematical test cases. Han et al. (2020) applied a deep convolutional residual neural network technique to emulate SP-CAM model for moist physics parameterization in GCMs.

These MMF works commonly employ different dynamics models (i.e., equation sets) for the LSP and SSP. In SSP modeling, an anelastic approximation is widely adopted to avoid numerical issues associated with fast-propagating acoustic waves (Grabowski, 2016); however, Arakawa and Konor (Arakawa & Konor, 2009) emphasized the necessity of a unified modeling approach for GCM and CRM to ensure consistency and provide flexibility in choosing resolution based on the objective of the applications. Kurowski et al. (2015) supported the suitability of compressible dynamics at global-scale modeling. Many MMF works have incorporated 2D CRMs for SSP modeling, motivated by reasonable success of early MMF works. While 2D CRMs are considered capable of representing cloud processes in each column of the large-scale model, as documented in Grabowski (2001), there are efforts to replicate 3D effects of SSP or directly implement 3D SSP models. Jung and Arakawa (Jung & Arakawa, 2010) proposed a quasi-3D CRM to couple with a GCM, where the SSP domains are narrow channels with a small thickness and embedded in perpendicular directions, achieving comparable results to a full 3D CRM. Jansson et al. (2019) presented a coupling scheme for OpenIFS and 3D DALES models in select regions, which were successfully integrated despite significant differences in terms of domain height, units for quantities, and prognostic variables.

This paper presents a novel MMF method designed for moist atmospheric limited-area simulations. The LSP and SSP models within the current MMF share the same dynamical core, employing consistent governing equations and discretization methods. Both models are constructed using the nonhydrostatic compressible Navier-Stokes equations with moisture and discretized by the element-based Galerkin method (e.g., see (Giraldo, 2020)). We use the Nonhydrostatic Unified Model of the Atmosphere (NUMA) (Kelly & Giraldo, 2012) as a base model for both LSP and SSP. To implement this MMF simulation, we have restructured the NUMA code into a fully object-oriented form, enabling the instantiation of numerous simulations (we call this new model xNUMA). We test the MMF method by applying it to two idealized limited-area weather problems: (a) a 2D squall line (Gaberšek et al., 2012) and (b) a 3D supercell thunderstorm (Tissaoui et al., 2023).

The element-based Galerkin method, specifically the spectral element method, has been adopted for the dynamical core of limited area models (LAMs) and GCMs for numerical weather prediction, as listed in Marras et al. (2016). Among the MMF models, SP-E3SM (Hannah et al., 2020) utilizes the spectral element method for its GCM. The element-based Galerkin method enables the adjustment of spatial resolution via element size (h-refinement) and the order of basis functions (p-refinement). It has demonstrated high-order accuracy and efficiency across various applications of dry and moist atmosphere (Gaberšek et al., 2012; Tissaoui et al., 2023; Yi & Giraldo, 2020). This paper represents the first application of the element-based Galerkin method for both LSP and SSP models for limited-area atmospheric MMF.

An outline of the paper is as follows. The governing equations for the nonhydrostatic moist atmosphere are presented in Section 2. Section 3 presents the coupling algorithm for the LSP and SSP model. Section 4 details the

numerical methods including the spatial and temporal discretizations, sponge layer, nonconforming vertical grids, and parallel implementation. The numerical test cases for the 2D squall line and 3D supercell are investigated in Section 5, and conclusions are drawn in Section 6. Appendix A provides the complexity of the algorithms for the standard and MMF simulations in terms of arithmetic intensity.

2. Governing Equations

Let us consider a fixed spatial domain Ω and a time interval $[0, t_f]$. The governing equations for the non-hydrostatic model of the moist atmosphere can be written as follows:

$$\frac{\partial \rho'}{\partial t} + \nabla \cdot \left((\rho_0 + \rho') \boldsymbol{u} \right) = 0, \tag{1a}$$

$$\frac{\partial \boldsymbol{u}}{\partial t} + \boldsymbol{u} \cdot \nabla \boldsymbol{u} + \frac{1}{\rho_0 + \rho'} \nabla p' + g\boldsymbol{k} \left(\frac{\rho'}{\rho_0 + \rho'} - \varepsilon q_v' + q_c + q_r \right) = \nu \nabla^2 \boldsymbol{u}, \tag{1b}$$

$$\frac{\partial \theta_v'}{\partial t} + \boldsymbol{u} \cdot \nabla \left(\theta_{v0} + \theta_v' \right) = S_{\theta_v'} + \nu \nabla^2 \theta_v', \tag{1c}$$

$$\frac{\partial q_v'}{\partial t} + \boldsymbol{u} \cdot \nabla \left(q_{v0} + q_v' \right) = S_v + \nu \nabla^2 q_v', \tag{1d}$$

$$\frac{\partial q_c}{\partial t} + \boldsymbol{u} \cdot \nabla q_c = S_c + \nu \nabla^2 q_c, \tag{1e}$$

$$\frac{\partial q_r}{\partial t} + \boldsymbol{u} \cdot \nabla q_r = S_r + \nu \nabla^2 q_r, \tag{1f}$$

where $\rho_0(z)$ is the reference density, ρ' is the density perturbation, $\boldsymbol{u}$ is the velocity vector, $\theta_{v0}(z)$ is the reference virtual potential temperature (VPT), θ_v' represents the VPT perturbation, p' is the pressure perturbation, g is the gravitational acceleration, $\boldsymbol{k}$ is the upward-pointing unit vector, $\varepsilon = R_v/R_d - 1 \approx 0.608$ with the specific gas constants of dry air and water vapor denoted by R_d and R_v, and ν is the kinematic viscosity. In the last three equations, q_v, q_c, and q_r represent the mixing ratios of water vapor, cloud water, and rain, respectively. Note that the reference variables, denoted by subscript 0, are functions of height z only. Equations 1a–1c represent local mass conservation, momentum balance, and thermodynamics, respectively. The transport of water species and moist microphysical processes are represented by, the latent heat release term $S_{\theta_v'}$ in Equation 1c, and the buoyancy terms in Equation 1b. We assume that the reference fields are in hydrostatic balance and dependent only on the vertical coordinate z, that is, $\frac{\mathrm{d}p_0}{\mathrm{d}z} = -\rho_0 g$. The source terms, $S_{\theta_v'}$, S_v, S_c, and S_r describe the effects of the microphysical processes, including condensation, autoconversion, accretion, evaporation, and sedimentation. These terms are defined using the Kessler microphysics model, as summarized in Klemp and Wilhelmson (1978) with the exception of the use of VPT variable.

In this work, we adopt VPT, θ_v, as a state variable, which is also used in most U.S. Navy NWP models, including the NAVy Global Environmental Model (NAVGEM) (Hogan et al., 2014; Hogan & Rosmond, 1991) and the Navy Environmental Prediction sysTem Utilizing a Nonhydrostatic Engine (NEPTUNE) (Zaron et al., 2022). Since NUMA serves as a testbed for these models, previous versions of NUMA have also used VPT for both 2D (Gaberšek et al., 2012) and 3D (Tissaoui et al., 2023) simulations of moist processes. VPT incorporates an exact moisture-modified gas constant (Eckermann et al., 2023) and consequently yields exact moisture-modified pressure gradient forces in the momentum balance, Equation 1b. Other moist nonhydrostatic models, such as (Bryan & Fritsch, 2002; Klemp & Wilhelmson, 1978), use (dry) potential temperature, θ or $\ln \theta$, respectively, as a state variable while invoking VPT in the equation of state and attendant pressure gradient force. Although the diabatic term $S_{\theta_v'}$ in Equation 1c differs from the source-sink terms in these models, both θ_v and θ are valid thermodynamic variables.

The prognostic variables for system Equation 1 are $\boldsymbol{q} = \left(\rho', \boldsymbol{u}^{\mathcal{T}}, \theta_v', q_v', q_c, q_r \right)^{\mathcal{T}}$, where the superscript $\mathcal{T}$ denotes the transpose operator. Equation 1 can be rewritten more concisely in the compact form as

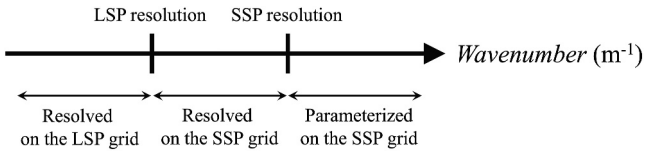

Figure 1. Decomposition of the scales modeled via MMF along the wavenumber axis.

$$\frac{\partial \boldsymbol{q}}{\partial t} = \mathcal{S}(\boldsymbol{q}), \tag{2}$$

where $\mathcal{S}(\boldsymbol{q})$ contains all terms in the equations apart from the time derivatives. The pressure of moist air is calculated using the thermodynamic equation of state

$$p = \rho R_d T_v, \tag{3}$$

where the virtual temperature T_v is defined as $T_v = T(1 + \varepsilon q_v)$, with the air temperature T (Vallis, 2005).

Let us now describe the MMF strategy that we use to solve the governing equations.

3. Multiscale Modeling Framework

We consider a limited-area domain for modeling the large-scale process (LSP) and local domains for modeling the small-scale processes (SSP) locally within each column of the LSP. Figure 1 illustrates the three regions of scales along the conceptual wavenumber axis that are handled differently in our MMF strategy. The LSP (such as the global circulation) is resolved on the LSP grid while the SSPs (such as cloud-scale processes) are explicitly resolved on the SSP grid. Subgrid-scale processes including precipitation microphysics are parameterized on the SSP grid. Since the parameterization is performed on a finer grid with the SSP resolution than in the standard simulation, it is expected that this will enhance accuracy in representing fine-scale features.

3.1. LSP and SSP Coupling

In order to couple the LSP and SSP models, we employ the coupling method used in the original super-parameterization scheme (Grabowski, 2001, 2004). Let us denote the LSP and SSP domains as Ω_{LSP} and Ω_{SSP}, with the prognostic variables for LSP and SSP represented as $\boldsymbol{Q}$ and $\boldsymbol{q}$, respectively. The LSP domain is discretized with low resolution as a global circulation model (GCM), while the SSP domains are discretized with high resolution as a cloud-resolving model (CRM), as shown in Figure 2. In this work, we consider a two-dimensional SSP model generated at each grid column of a 2D or 3D LSP model. For three-dimensional problems, the SSP domains align with the background wind direction; in what follows, we assume this direction to be along the Cartesian x-direction. The coupling condition that is imposed is

$$\boldsymbol{Q}(X, Y, Z, t) = \langle \boldsymbol{q}(x, y, z, t) \rangle|_{(X,Y)}, \tag{4}$$

which dictates that the LSP variable equals the horizontal average of the SSP variable for each level in the LSP column. We assume periodicity in the horizontal direction (Grabowski, 2001). Therefore, this SSP model represents the small-scale processes that occur around each LSP column. The two-dimensional horizontal averaging operator $\langle \cdot \rangle|_{(X,Y)}$ is defined as

$$\langle \boldsymbol{q}(x, 0, z, t) \rangle|_{(X,Y)} = \frac{1}{L_x} \int_{-L_x/2}^{L_x/2} \boldsymbol{q}(\xi, 0, z, t)|_{(X,Y)} d\xi, \tag{5}$$

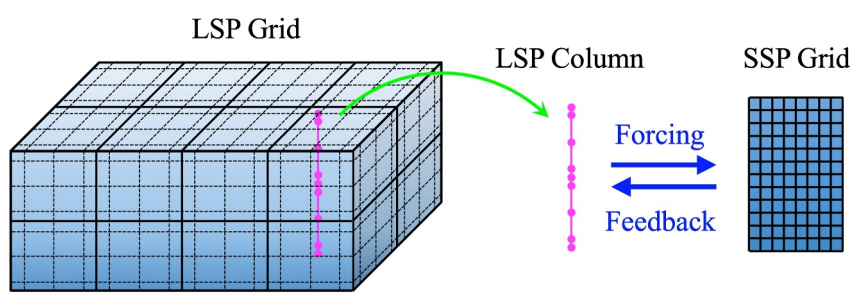

Figure 2. Configuration of the LSP and SSP grids for MMF.

where L_x is the length of the SSP domain in the x direction.

The LSP and SSP models are coupled in two ways. LSP variables drive the flows in the SSP models through a forcing term, and each LSP column receives feedback from the corresponding SSP models. The coupling of the LSP and SSP models is achieved by adding forcing or feedback terms to the governing Equation 2, resulting in the following coupled model:

$$\frac{\partial \boldsymbol{Q}}{\partial t} = \bar{\mathcal{S}}(\boldsymbol{Q}) + \boldsymbol{F}(\boldsymbol{Q},\boldsymbol{q}) \tag{6}$$

$$\frac{\partial \boldsymbol{q}}{\partial t} = \tilde{\mathcal{S}}(\boldsymbol{q}) + \boldsymbol{f}(\boldsymbol{q},\boldsymbol{Q}), \tag{7}$$

where $\bar{\mathcal{S}}(\boldsymbol{Q})$ and $\tilde{\mathcal{S}}(\boldsymbol{q})$ are the operators for the LSP and SSP models, respectively. We use the same governing equations for modeling both LSP and SSP, with the exception of the microphysical source terms $S_{\theta_v'}$, S_v, S_c, and S_r in Equation 1, which are included only in $\tilde{\mathcal{S}}(\boldsymbol{q})$. Consequently, the MMF proposed in this work yields a non-hydrostatic model for both LSP and SSP and a mathematically consistent method in the treatment of the large-scale and small-scale features.

3.2. Temporal Discretization

To simplify the exposition of the time-discretization, in what follows let us assume we are only using first order Runge-Kutta (RK) methods (e.g., forward and backward Euler methods); however, it should be understood that we may use any order RK method as described in Giraldo et al. (2013). The update of LSP and SSP variables progresses from time level n to $n + 1$ over the LSP time step ΔT using an implicit-explicit (IMEX) time integrator (Giraldo et al., 2013) as follows:

$$\boldsymbol{Q}^{n+1} = \boldsymbol{Q}^n + \Delta T\left[\bar{\mathcal{S}}_\delta\left(\boldsymbol{Q}^n,\boldsymbol{Q}^{n+1}\right) + \boldsymbol{F}^n\left(\boldsymbol{Q}^n,\boldsymbol{q}^n\right)\right], \tag{8}$$

$$\boldsymbol{q}^{n+1} = \boldsymbol{q}^n + \sum_{m=1}^{M} \Delta t\left[\tilde{\mathcal{S}}_\delta\left(\boldsymbol{q}^{n+(m-1)/M},\boldsymbol{q}^{n+m/M}\right) + \boldsymbol{f}^n\left(\boldsymbol{q}^n,\boldsymbol{Q}^{n+1}\right)\right], \tag{9}$$

where Δt is the SSP time step, $M = \Delta T/\Delta t$ is the number of SSP time steps per LSP time step, and the subscript δ indicates the IMEX operator defined as $\mathcal{S}_\delta\left(\boldsymbol{Q}^n,\boldsymbol{Q}^{n+1}\right) = [\mathcal{S}(\boldsymbol{Q}^n) - \delta\mathcal{L}(\boldsymbol{Q}^n)] + \delta\mathcal{L}\left(\boldsymbol{Q}^{n+1}\right)$ with the linear operator $\mathcal{L}$ given in Giraldo et al. (2013) and the parameter $\delta \in \{0,1\}$ switches the formulation between forward Euler and linear IMEX. The forcing term $\boldsymbol{F}^n$ and the feedback term $\boldsymbol{f}^n$ are defined as follows:

$$\boldsymbol{F}^n\left(\boldsymbol{Q}^n,\boldsymbol{q}^n\right) = \frac{\langle \boldsymbol{q}^n\rangle - \boldsymbol{Q}^n}{\Delta T}, \tag{10}$$

$$\boldsymbol{f}^n\left(\boldsymbol{q}^n,\boldsymbol{Q}^{n+1}\right) = \frac{\boldsymbol{Q}^{n+1} - \langle \boldsymbol{q}^n\rangle}{\Delta T}, \tag{11}$$

where $\boldsymbol{q}^n$ denotes the SSP state variables from the previous time step n, while $\boldsymbol{Q}^n$ and $\boldsymbol{Q}^{n+1}$ are the LSP state variables from the previous time step n and the current time step $n + 1$, respectively. Equations 10 and 11 introduce tendencies that relax each LSP state variable toward their SSP counterparts and vice versa, ensuring that both do not drift appreciably during time integration. Both Equations 10 and 11 will vanish if the coupling condition in Equation 4 is exactly satisfied at each time step.

In the IMEX method, the terms responsible for fast waves, such as acoustic and gravity waves, are discretized implicitly, while the other terms for slower dynamics are discretized explicitly. This IMEX strategy enables the use of larger time steps by eliminating the tight CFL restriction due to the fast waves. In this work, we employ the second-order additive Runge-Kutta (ARK2) scheme proposed in Giraldo et al. (2013), which belongs to a family of linear multistage schemes. This time integrator is also used in Giraldo et al. (2024) referred to as ARK (2,3,2)b. We solve the linear system that arises from the implicit part of the IMEX formulation using the iterative Krylov

subspace GMRES (Saad & Schultz, 1986) in a matrix-free fashion. While the MMF method offers flexibility in selecting different time integrators for LSP and SSP models, we choose to use the same time integrators for both models in MMF simulations in this work. Future work could explore the use of different time integrators and orders of accuracy for the SSP models.

3.3. Implementation Details

We couple the LSP and SSP models in terms of horizontal velocity, VPT, and the mixing ratios of water vapor, cloud water, and rain; density and vertical velocity are not coupled. The idea here is to mimic as closely as possible the procedure used with a standard parameterization. We consider grid refinement primarily in the horizontal direction via the MMF but also in the vertical direction using the nonconforming vertical discretization described in Section 4.4. Consequently, the forcing and feedback terms in Equations 10 and 11 are added to the right-hand side of the corresponding balance equations in Equation 1.

To ensure an adequate representation of spatial scales at the LSP resolution, as shown in Figure 1, it is necessary to select an SSP domain size large enough to capture the largest wavenumber (smallest wavelength) that can be resolved at the LSP resolution.

Algorithm 1 presents the pseudocode for the time integration loop in the MMF. The outermost loop iterates over time steps for the LSP model. During each time step, we begin by updating the LSP state variables $\boldsymbol{Q}$ by integrating Equation 6. Afterward, we update the SSP state variables $\boldsymbol{q}$ within each SSP domain through multiple subtime steps. A smaller time-step size may be necessary for the SSP due to its finer grid resolution and CFL constraint. In principle, we have the flexibility to choose different time-integration methods to independently handle the stability and efficiency of the LSP and SSP models. The numerical test case in Section 5.1 demonstrates that these staggered updates impose the coupling conditions accurately. This staggered approach also reduces computational overhead. In distributed-memory parallel computations, inter-processor communication is required only during the LSP update, while the subsequent SSP updates occur on-process.

Algorithm 1. Time integration loop, where *nstep* is the number of time steps in the LSP model, M is the number of SSP time steps per LSP time step, and the coefficient $\delta \in \{0, 1\}$ determines whether the time-integration method is explicit or IMEX.

for $n = 1, nstep$ **do**
  Update LSP state variables: $\boldsymbol{Q}^{n+1} = \boldsymbol{Q}^{n} + \Delta T\left[\overline{S}_{\delta}\left(\boldsymbol{Q}^{n}, \boldsymbol{Q}^{n+1}\right) + \frac{\langle \boldsymbol{q}^{n} \rangle - \boldsymbol{Q}^{n}}{\Delta T}\right]$.
  for $m = 1, M$ **do**
    Update SSP state variables:
    $\boldsymbol{q}^{n+m/M} = \boldsymbol{q}^{n+(m-1)/M} + \Delta t\left[\tilde{S}_{\delta}\left(\boldsymbol{q}^{n+(m-1)/M}, \boldsymbol{q}^{n+m/M}\right) + \frac{\boldsymbol{Q}^{n+1} - \langle \boldsymbol{q}^{n} \rangle}{\Delta T}\right]$.
    Update SSP state variables by the contribution of the source term.
  end for
end for

4. Numerical Methods

This section describes the numerical methods employed in our limited-area simulations using the standard and MMF approaches. In the MMF, we use the continuous version of the element-based Galerkin method (spectral elements) (Giraldo, 2020) to spatially discretize both the LSP and SSP domains. We add the microphysics model to parameterize the SSP models. An implicit sponge layer (Klemp et al., 2008) serves as an upper absorbing boundary condition (ABC). The coupling of the LSP and SSP grids accommodates nonconforming discretization in the vertical direction. Section 4.5 describes the parallel implementation of our MMF simulations. The complexity of the algorithms for the standard and MMF simulations is discussed in Appendix A.

4.1. Element-Based Galerkin Method

The element-based Galerkin method decomposes the spatial domain $\Omega \subset \mathbb{R}^d$ ($d = 2$ or 3) into N_e disjoint elements Ω_e such as $\Omega = \bigcup_{e=1}^{N_e} \Omega_e$. In our model, the Ω_e are either quadrilaterals (in 2D) or hexahedra (in 3D). Within each element Ω_e, the prognostic vector $\boldsymbol{q}$ is approximated as a finite-dimensional projection $\boldsymbol{q}_N$ using basis functions $\psi_j(\boldsymbol{x})$ and element-wise nodal coefficients $\boldsymbol{q}_j^{(e)}(t)$ such that

$$\boldsymbol{q}_N(\boldsymbol{x}, t) = \sum_{j=1}^{M_N} \psi_j(\boldsymbol{x}) \boldsymbol{q}_j^{(e)}(t), \tag{12}$$

where N denotes the order of the basis functions, $M_N = (N + 1)^d$ is the number of nodes per element, and the superscript (e) denotes element-wise quantities. The basis functions are constructed as tensor products of N-th order Lagrange polynomials h_α associated with the Legendre-Gauss-Lobatto (LGL) points, given by

$$\psi_i(\xi, \eta, \zeta) = h_\alpha(\xi) \otimes h_\beta(\eta) \otimes h_\gamma(\zeta), \tag{13}$$

where $\alpha, \beta, \gamma \in \{1, \ldots, N + 1\}$, and (ξ, η, ζ) are the element coordinates in the reference domain $E = [-1, 1]^d$ that are mapped from the physical coordinate $\boldsymbol{x}$ via metric terms.

For a continuous Galerkin (CG) method, let us consider a finite-dimensional Sobolev space $\mathcal{V}_\mathcal{N}$ defined as

$$\mathcal{V}_\mathcal{N} = \{\psi \mid \psi \in H^1(\Omega) \text{ and } \psi \in \mathcal{P}_N(\Omega_e)\}, \tag{14}$$

where $\mathcal{P}_N(\Omega_e)$ is the set of all polynomials of degree less than or equal to N on the element Ω_e. The discrete weak form of the governing equation in Equation 2 is obtained by multiplying it by a test function and integrating over the domain, which is stated as follows: Find $\boldsymbol{q}_N \in \mathcal{V}_\mathcal{N}$ such that for all $\psi \in \mathcal{V}_\mathcal{N}$,

$$\sum_{e=1}^{N_e} \int_{\Omega_e} \psi_i \frac{\partial \boldsymbol{q}_N}{\partial t} \, d\Omega_e = \sum_{e=1}^{N_e} \int_{\Omega_e} \psi_i \mathcal{S}(\boldsymbol{q}_N) \, d\Omega_e. \tag{15}$$

In 3D, the integral over the domain Ω is computed using a quadrature rule based on the LGL points as follows:

$$\int_\Omega (\cdot) \, d\Omega = \sum_{e=1}^{N_e} \int_{\Omega_e} (\cdot) \, d\Omega_e \approx \sum_{e=1}^{N_e} \sum_{i=1}^{N_\xi+1} \sum_{j=1}^{N_\eta+1} \sum_{k=1}^{N_\zeta+1} w_{ijk}^{(e)} J_{ijk}^{(e)}(\cdot), \tag{16}$$

where N_ξ, N_η, and N_ζ are the orders of polynomial basis functions in each direction, and $w_{ijk}^{(e)}$ and $J_{ijk}^{(e)}$ denote the weight and Jacobian determinant associated with the LGL points, respectively.

The discrete weak form in Equation 15 yields a matrix-vector form written as

$$M_{IJ} \frac{\mathrm{d}\boldsymbol{q}_J}{\mathrm{d}t} = R_I(\boldsymbol{q}_N), \tag{17}$$

where $I, J \in \{1, \ldots, N_p\}$ and N_p is the total number of global grid points, and the standard summation convention is assumed unless otherwise specified. The global mass matrix M_{IJ} and the right-hand side (RHS) vector R_I are constructed by applying the global assembly or direct stiffness summation (DSS) operator $\bigwedge_{e=1}^{N_e}$ to the element-wise mass matrices and RHS vectors as follows:

$$M_{IJ} = \bigwedge_{e=1}^{N_e} \int_{\Omega_e} \psi_i(\boldsymbol{x}) \psi_j(\boldsymbol{x}) \, d\Omega_e, \tag{18}$$

$$R_I(\boldsymbol{q}_N) = \bigwedge_{e=1}^{N_e} \int_{\Omega_e} \psi_i(\boldsymbol{x}) \mathcal{S}(\boldsymbol{q}_N)\, d\Omega_e, \tag{19}$$

where the DSS operator performs summation through mapping from local indices to global indices as $(i,e) \rightarrow I$ and $(j,e) \rightarrow J$. We choose the integration points to be co-located with the interpolation points (inexact integration), which yields accurate numerical integration for $N \geq 4$ (Giraldo, 1998). This choice makes the mass matrix M_{IJ} diagonal due to the cardinal property of the basis functions, simplifying inversion. Consequently, we obtain

$$\frac{\mathrm{d}\boldsymbol{q}_I}{\mathrm{d}t} = M_I^{-1} R_I(\boldsymbol{q}_N). \tag{20}$$

Equation 20 is used to calculate the solutions for both the LSP and SSP problems in the MMF simulations, where $\mathcal{S}$ in Equation 19 is augmented with the corresponding coupling term, $\boldsymbol{F}$ or $\boldsymbol{f}$ given in Equations 10 and 11. The element-based Galerkin methods used in this work ensure conservation of global mass, as the continuity equation for density is written in a conservative form (Giraldo, 2020). Supporting numerical evidence was provided in our earlier paper (Giraldo et al., 2024).

4.2. Microphysics Model

For modeling the Kessler microphysics, the microphysical source terms on the right-hand side are present only in the SSP model. Meanwhile, the LSP model transports the mixing ratios for the three species of water. The microphysical source terms in Equation 1 have been implemented in the NUMA model (Giraldo et al., 2013) using both the column-based approach (Gaberšek et al., 2012) and the non-column-based approach (Tissaoui et al., 2023). We adopt the column-based approach for modeling moist microphysics in this work, since we use vertical columns to couple the LSP and SSP models.

While the only additional sources we include exclusively in the SSP model are the microphysical terms $S_{\theta_v'}$, S_v, S_c, and S_r, it is important to consider whether the LSP or SSP should account for other sources (e.g., surface fluxes). We refer interested readers to the other MMF papers that discuss their decisions on this topic (Hannah et al., 2020; Jansson et al., 2019). In addition, the current model does not include a turbulence parameterization or subgrid-scale mixing scheme but incorporates artificial diffusion to control numerical instability.

4.3. Implicit Sponge Layer

NWP models commonly require a non-reflecting boundary condition at the top of the domain to mimic the infinite vertical extent of the atmosphere. We employ the implicit Rayleigh damping technique (Klemp et al., 2008) for absorbing upper gravity waves. This method adds a damping term only to the vertical momentum balance in Equation 1b, unlike traditional gravity wave absorbers, as follows:

$$\frac{\partial \boldsymbol{u}}{\partial t} = \mathcal{S}_{\boldsymbol{u}}(\boldsymbol{q}) - R_w(z)\left(\boldsymbol{k}\boldsymbol{k}^T\right)\boldsymbol{u}, \tag{21}$$

where $\mathcal{S}_{\boldsymbol{u}}(\boldsymbol{q})$ represents the operators in the momentum balance equations, $\boldsymbol{k}$ is the upward-pointing unit vector, $\boldsymbol{k}\boldsymbol{k}^T$ is an orthogonal projector, and the vertically varying damping profile $R_w(z)$ is defined as

$$R_w(z) = R_{\max} \sin^2\left[\frac{\pi}{2}\left(\frac{z - z_b}{z_t - z_b}\right)\right], \tag{22}$$

where z is the vertical coordinate, z_b is the height at the bottom of the sponge layer, z_t is the model top, and the coefficient $R_{\max}$ controls the magnitude of the damping to minimize the reflection while maximizing absorption. Like the buoyancy term, the damping term is treated implicitly in our IMEX scheme. Since no damping is applied

to the continuity Equation 1a, this scheme preserves local mass conservation. We use a thickness ($\Delta z_s = z_t - z_b$) of 6 km and $R_{\max} = 0.25\ \mathrm{s}^{-1}$ at the top to absorb the gravity and acoustic waves (Klemp et al., 2008) for the standard simulation and LSP/SSP models in MMF simulations of the squall line and supercell in Section 5.

4.4. Nonconforming Vertical Grids

Our MMF method allows the coupling of nonconforming vertical discretizations of LSP and SSP models. This capability is incorporated into the MMF models to achieve grid refinement effects not only in the horizontal direction but also in the vertical. This flexibility is particularly useful when the LSP and SSP grids have a different number of elements or different order of basis functions in the vertical. The coupling of the LSP and SSP variables, evaluated in different spaces, is achieved by projecting them onto their counterpart spaces using the element-wise least-squares projection. This projection method is adopted from the adaptive mesh refinement strategy for the element-based Galerkin method (Giraldo, 2020; Kopera & Giraldo, 2014, 2015; Kopriva, 1996, 2009).

Let us consider a 1D domain, $[0, z_{\text{top}}]$, corresponding to the columns of LSP and SSP grids. Each column of the LSP and SSP model is discretized using 1D spectral elements. We assume that an LSP element is divided by multiple SSP elements, where the number of SSP elements per LSP element is denoted by $N_{S/L} \geq 1$. Let $\hat{\zeta}$ and $\tilde{\zeta}$ denote the natural coordinates on the LSP and SSP elements along the vertical axis in the reference element, respectively, and $\hat{\psi}$ and $\tilde{\psi}$ denote the basis functions of the LSP and SSP elements, respectively. The following relationship between the natural coordinates on the LSP and SSP elements holds:

$$\hat{\zeta} = s\tilde{\zeta}^{(k)} + o^{(k)} \quad (k = 1, \ldots, N_{S/L}), \tag{23}$$

where the coefficients are determined by $s = 1/N_{S/L}$ and $o^{(k)} = (2k - 1)s - 1$.

The projections between the LSP and SSP variables are defined as

$$Q_i = P_{ij}^{S\to L} q_j, \tag{24a}$$

$$q_i = P_{ij}^{L\to S} Q_j. \tag{24b}$$

The element-wise projection matrices are defined as

$$P_{ij}^{S\to L} = \hat{M}_{ik}^{-1}\left(\int_{-1}^{1} \hat{\psi}_k \tilde{\psi}_j d\hat{\zeta}\right), \tag{25a}$$

$$P_{ij}^{L\to S} = \tilde{M}_{ik}^{-1}\left(\int_{-1}^{1} \tilde{\psi}_k \hat{\psi}_j d\tilde{\zeta}\right), \tag{25b}$$

where $\hat{M}_{ij} = \int_{-1}^{1} \hat{\psi}_i \hat{\psi}_j d\hat{\zeta}$ and $\tilde{M}_{ij} = \int_{-1}^{1} \tilde{\psi}_i \tilde{\psi}_j d\tilde{\zeta}$ are 1D mass matrices. The matrices in the parenthesis in Equations 25a and 25b are calculated as follows:

$$\int_{-1}^{1} \hat{\psi}_i \tilde{\psi}_j d\hat{\zeta} = s \sum_{k=1}^{N_{S/L}} \hat{\psi}_i\left(s\tilde{\zeta}_j^{(k)} + o^{(k)}\right) w_j, \tag{26a}$$

$$\int_{-1}^{1} \tilde{\psi}_i \hat{\psi}_j d\tilde{\zeta} = \hat{\psi}_j\left(s\tilde{\zeta}_i^{(k)} + o^{(k)}\right) w_i, \tag{26b}$$

where w_i is the weight of the quadrature rule. Consequently, the projection matrices $P_{ij}^{S\to L}$ and $P_{ij}^{L\to S}$ are not square, and their dimensions are $(N + 1) \times N_{S/L}(N + 1)$ and $N_{S/L}(N + 1) \times (N + 1)$, respectively, where N is the order of the basis functions.

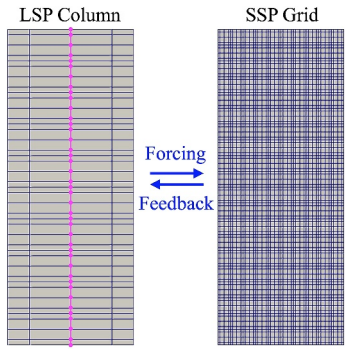

Figure 3. Coupling of nonconforming LSP and SSP grids for the MMF.

Figure 3 illustrates an example of nonconforming LSP and SSP grids. In this figure, the LSP and SSP grids have 5 and 10 elements in the vertical direction, respectively, both with fourth order basis functions. Consequently, $N_{S/L} = 2$ at each LSP column.

To verify whether the LSP and SSP simulations are properly coupled, we compared the horizontal velocity and potential temperature profiles along the vertical line at the center of the LSP grid and its corresponding SSP for the test case described in Section 5.1. As a result, the two curves of the LSP and SSP overlap each other (not shown), which demonstrates the accurate imposition of the coupling condition in Equation 4 despite the difference in the vertical grid spacing in the LSP and SSP grids.

4.5. Parallel Implementation

This section describes our parallel implementation of the numerical methods for the MMF simulations. The MMF simulation instantiates a single LSP simulation and multiple SSP simulations simultaneously. Each LSP and SSP simulation utilizes the dynamical core of NUMA (Giraldo et al., 2013; Kelly & Giraldo, 2012). To facilitate this task, we developed an object-oriented version of NUMA with multiple, independent simulator objects which we call xNUMA. Each simulator object contains objects for input, spatial discretization, time integration, and solvers. Consequently, all the data and functions that constitute a simulation are members of the simulator objects.

The current MMF model is implemented via distributed memory parallelism using MPI. We subdivide the LSP domain for limited-area simulations into multiple subdomains of equal size using non-overlapping element-based partitioning. In this configuration, each element is exclusively assigned to a single partition, and each partition is assigned to an MPI process (or core). As a result, workload is well balanced among MPI processes. As we adopt the column-based model for moist microphysics, these partitions encompass all grid points and elements in the vertical direction. Figure 4 illustrates three types of layouts for domain decomposition. An SSP grid is generated at each column, resulting in a total $N_{p,x} \times N_{p,y}$ of SSP simulations for an MMF simulation, where $N_{p,x}$ and $N_{p,y}$ are the number of grid points in the x and y directions. Each SSP simulator runs serially on the MPI process that contains the corresponding LSP column, and consequently, the communication between the LSP and SSP models only occur within each processor. In the MMF model, inter-process communications are required only for the global DSS operation over the LSP partitions. Therefore, the communication load for the MMF model is significantly lower than that of the standard model for the same grid size, as discussed in Section A2.

The parallelization of the LSP model is similar to what we implemented for the standard model. Details about the computational stencil for the element-based Galerkin method and the global DSS process can be found in Kelly and Giraldo (2012).

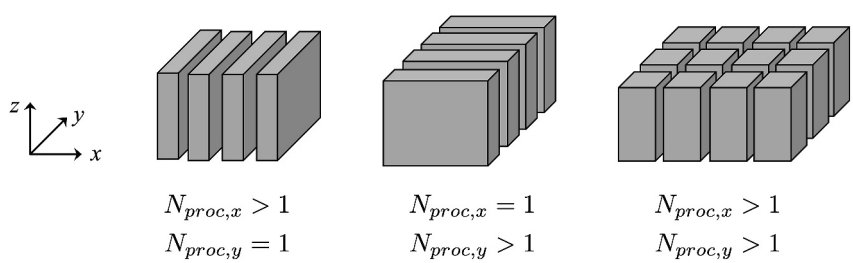

Figure 4. Layouts of domain decomposition for limited-area models. ($N_{proc,x}$ and $N_{proc,y}$ are the number of processor elements in the x and y directions).

A motivation for MMF from a computing perspective is to achieve more efficient parallelism. Numerical atmospheric models tend to be limited in performance due to being memory-bandwidth-bound rather than compute-bound in distributed memory parallelism. This has been a bottleneck in fully exploiting massively parallel systems, such as graphics processing units (GPUs). Therefore, numerical algorithms that require more computations but less memory communication will be favorable for such computer architectures. For this objective, an MMF strategy is attractive since it offloads computations from the parallel LSP to the serial SSPs, while keeping inter-process communications only at the level of the LSP model. The coupling of LSP and SSP models is achieved through column-wise profiles, which requires minimal memory access. As modern high-performance computing (HPC) increasingly shifts toward GPU-based machines, an MMF strategy becomes a promising pathway. To this end, we analyze the computational complexity of both the MMF and standard algorithms in Appendix A.

5. Numerical Results

We test the MMF method on two benchmark problems in numerical weather modeling. In this section, we refer to the simulations without the use of the MMF approach as standard simulations. We assess the performance of the MMF simulation by comparing it with these standard simulations. For the standard simulations, we consider two levels of resolution: a coarse one matching the resolution of the GCM, which is similar to the resolution of the LSP model in the MMF, and a fine one at a much higher resolution for the CRM, akin to the resolution of the SSP model in the MMF. In the element-based Galerkin method described in Section 4.1, the collocation points are not evenly distributed within a spectral element. Therefore, we define the equivalent grid size as $\Delta x = h/N$, where h is the width of spectral element and N is the order of the basis function. This definition represents the averaged horizontal distance between two points in the grid.

The simulations were conducted using 2.0 GHz AMD EPYC 7662 64-Core processors on the NPS (Naval Postgraduate School) Supercomputer. For parallel runs of the MMF simulation, each element column is assigned to a single core. As a result, we use 18 cores for the MMF squall line and 216 cores for the MMF supercell case, matching the number of element columns in the LSP domains.

5.1. 2D Squall Line

We test the MMF method using the squall line test case (Gaberšek et al., 2012; Tissaoui et al., 2023), an idealized benchmark weather problem. This test case has been used in previous studies on superparameterization and MMF methods (Majda & Grooms, 2014; Majda & Xing, 2010; Xing et al., 2009). The computational domain is a 2D channel with a horizontal length of 150 km and a height of 24 km. The x axis is in the streamwise direction, and the z axis is in the vertical direction. We impose impermeable boundary conditions at the bottom and periodic boundary conditions at the lateral boundaries. Additionally, we apply an implicit sponge layer as described in Section 4.3. The domain is spatially discretized using fourth-order basis functions. In the horizontal direction, the grid size is approximately 200 m for the standard fine grid and approximately 4.2 km for the standard coarse grid. The grid size in the vertical direction is approximately 200 and 400 m for the standard fine and coarse grids, respectively. The governing equations are integrated in time from $t \in [0, 8]$ hrs using the semi-implicit second-order additive Runge-Kutta (ARK2) method (Giraldo et al., 2013) with a time-step size of $\Delta t = 0.2$ s for the fine simulation and $\Delta T = 2$ s for the coarse simulation. An artificial viscosity with $\nu = 200$ m^2/s is added to the model, which is consistent with (Gaberšek et al., 2012; Tissaoui et al., 2023). The Boyd-Vandeven filter (Boyd, 1996) is applied with strength of 1%.

For the MMF simulation, the LSP domain retains the same dimensionality as the standard simulations, while the SSP grids are generated at every LSP grid column, each with a length of 8 km and a height of 24 km. The LSP domain is discretized with the same spatial and temporal resolutions as the standard coarse grid, while the SSP domain is discretized the same as the standard fine grid. Consequently, the LSP and SSP grids have different resolutions in the vertical direction, and there are 10 sub-steps for SSP per single LSP time step. An equal amount of artificial viscosity is added to both the LSP and SSP models, and the same filter is added to the LSP model. We set up the LSP simulation identically to the standard coarse simulation to examine the properties of the MMF simulation enriched by the SSP models. Table 1 summarizes the domain sizes and grid resolutions for the three simulations.

Table 1
Domain Size and Grid Resolution for the Squall Line Simulations

			MMF	
	Standard fine	Standard coarse	LSP	SSP
Domain Size (km)	150 × 24	150 × 24	150 × 24	8 × 24
Δx (m)	200	4,200	4,200	200
Δz (m)	200	400	400	200
Δt (sec)	0.2	2.0	2.0	0.2
Number of grid points	140,250	3,375	3,375	303,750 (45 simulations)
Number of time steps	144,000	14,400	14,400	144,000

The initial state consists of the reference field for a saturated boundary layer and a thermal perturbation. The reference fields of wind velocity, temperature, and the mixing ratio of water vapor are obtained from the atmosphere sounding data provided in the appendix of Tissaoui et al. (2023). The potential temperature perturbation at the initial time θ_0 is defined as follows:

$$\theta_v' = \begin{cases} \theta_c \cos^2\left(\frac{\pi r}{2}\right) & r < r_c, \\ 0 & r \geq r_c, \end{cases} \tag{27}$$

where

$$r = \sqrt{\left(\frac{x - x_c}{r_x}\right)^2 + \left(\frac{z - z_c}{r_z}\right)^2}, \tag{28}$$

and the parameters are set as $\theta_c = 3$ K, $r_c = 1$, $x_c = 75$ km, $z_c = 2$ km, $r_x = 10$ km, and $r_z = 1.5$ km, respectively. The SSP models are initialized with the profiles of the total variables along the corresponding LSP column. Consequently, the initial states of the SSP models are horizontally uniform. Additionally, we perturb these horizontally uniform potential temperature fields within the SSP models using a uniform random variable with amplitude of 0.3 K. This random perturbation is necessary to generate small-scale convection, as discussed in Grabowski (2001), and is defined as follows:

$$\theta_{\text{rand}} = (0.3\ \text{K})\frac{\theta_v'}{\theta_c} U, \tag{29}$$

where U is a uniform random variable on $[-1, 1]$, resulting in $-0.3\ \text{K} \leq \theta_{\text{rand}} \leq 0.3\ \text{K}$. We chose the amplitude used in Grabowski (2001).

In the MMF simulation, the relative mass loss in the LSP domain is maintained at machine double precision, that is, below 10^{-15}, throughout the entire simulation—confirming that the mass conservation property of the Galerkin formulation holds, even though the vertical discretization of the LSP and SSP models is non-conforming.

Figure 5 shows snapshots of the instantaneous VPT perturbations along with the cloud and rain mixing ratio contours at $t = 1500$, 3000, 6000, and 9000 s, illustrating the evolution of the storm. We display VPT perturbations following the precedent publications (Gaberšek et al., 2012; Tissaoui et al., 2023). The thermal bubble ascends, forming several cloud towers that merge into a large cloud cell. These clouds are convected eastward by the prevailing background wind. The evolution of the storm, particularly the cloud water, is highly dependent on the horizontal resolution. It is observed that the MMF produces cloud patterns closer to those of the standard fine (SF) simulation than the standard coarse (SC) simulation. This is particularly noticeable in the shape of the cloud cell in an updraft region at $t = 3000$ s and the cloud anvil at $t = 9000$ s. The MMF exhibits a slightly delayed

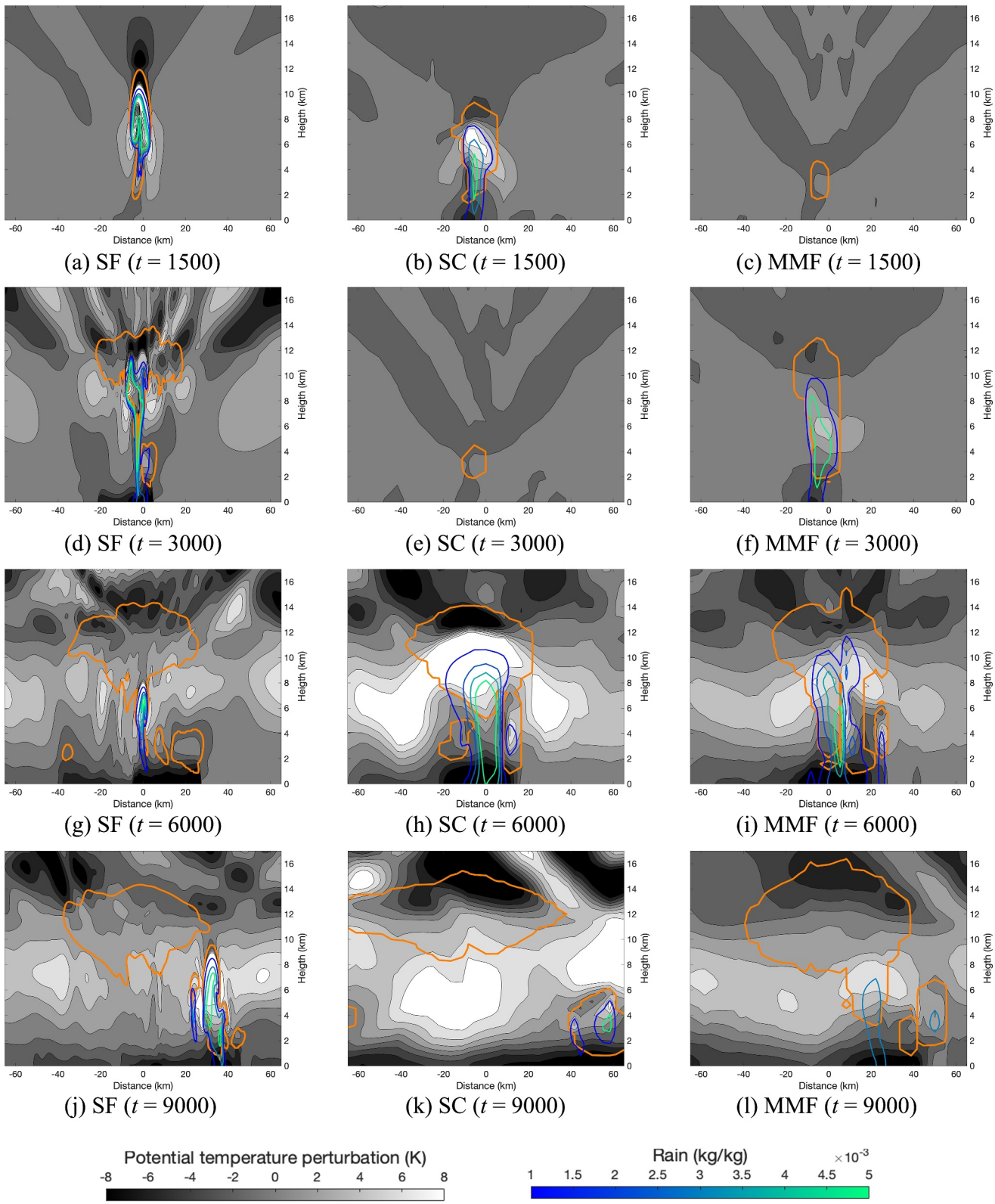

Figure 5. Instantaneous VPT perturbations at t = 1500 s (a-c), 3000 s (d-f), 6000 s (g-i), and 9000 s (j-l), computed from the standard fine (SF), standard coarse (SC), and MMF simulations for the squall line. The orange-colored line represents the contour of the cloud mixing ratio at $q_c = 10^{-5}$ kg/kg and the lines colored in blue-green scale present the contours of the rain mixing ratio.

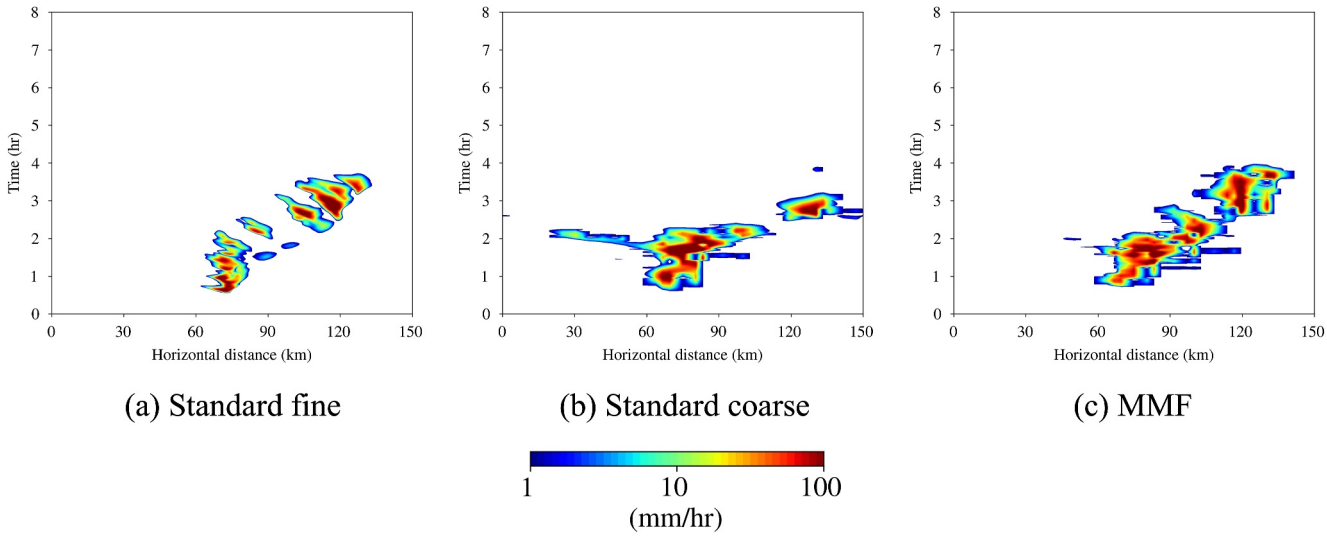

Figure 6. Contours of the surface precipitation in the squall line, computed from the standard fine (a), standard coarse (b), and MMF (c) simulations.

progression in the cloud processes, for example, the separation of stratiform clouds in the convective region is less distinct at $t = 6000$ compared to the SF.

Figure 6 illustrates contours of the surface precipitation on the space-time plane to show the propagating squall line from three different simulations: the standard simulations using fine and coarse grids and the MMF simulation. The pattern of surface precipitation from the MMF simulation is similar to that of the standard coarse and fine simulations. Rainfall occurs in two modes: convective precipitation is driven by strong updrafts and is intense but localized, while stratiform precipitation is more widespread and steady. In all three simulations, convective precipitation is dominant, while stratiform precipitation is not clearly distinguishable.

Figure 7 compares the distributions of the rain accumulation computed from the three simulations. The standard fine grid simulation yields a narrow and centered profile, while the standard coarse grid simulation produces a wide-spread profile. The profile of the MMF case is closer to the standard fine grid case in terms of shape. This result suggests the possibility that the MMF enhances accuracy in predicting the surface precipitation.

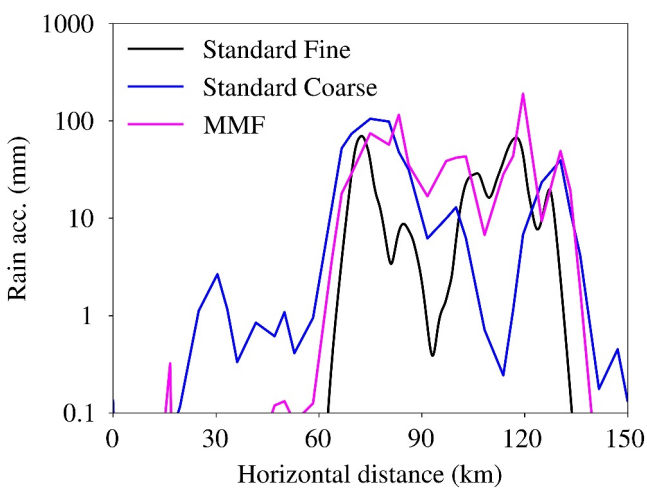

Figure 7. Distribution of the rain accumulation at $t = 8$ hrs for the squall line.

One of the key features in cloud processes is the cold pool (Rotunno et al., 1988), which is a cold pocket of air formed underneath a storm cloud. To identify the cold pool pattern in the simulations, the contours of the VPT perturbations at the surface are plotted in Figure 8. The MMF captures patterns of cold pools similarly to the fine simulation despite a much larger grid spacing, while the standard coarse simulation produces a wider distribution of cold pools.

Figure 9 compares the averaged kinetic energy computed from the three types of simulations. An ensemble of 20 MMF simulations were run, where the SSPs are randomly perturbed by Equation 29. This ensemble size corresponds to the FNMOC's operational ensemble size for NAVGEM (Hogan et al., 2014). The averaged kinetic energy per volume is defined as

$$\mathrm{KE} = \frac{\int_\Omega \frac{1}{2}\rho|\boldsymbol{u}|^2\, d\Omega}{\int_\Omega d\Omega}, \tag{30}$$

and the integral is computed as in Equation 16. In comparison to the standard fine case, the amplitude of the primary peak in the standard coarse case is much greater. In contrast, the MMF closely matches the kinetic energy profile of the fine simulation in terms of amplitude and pattern.

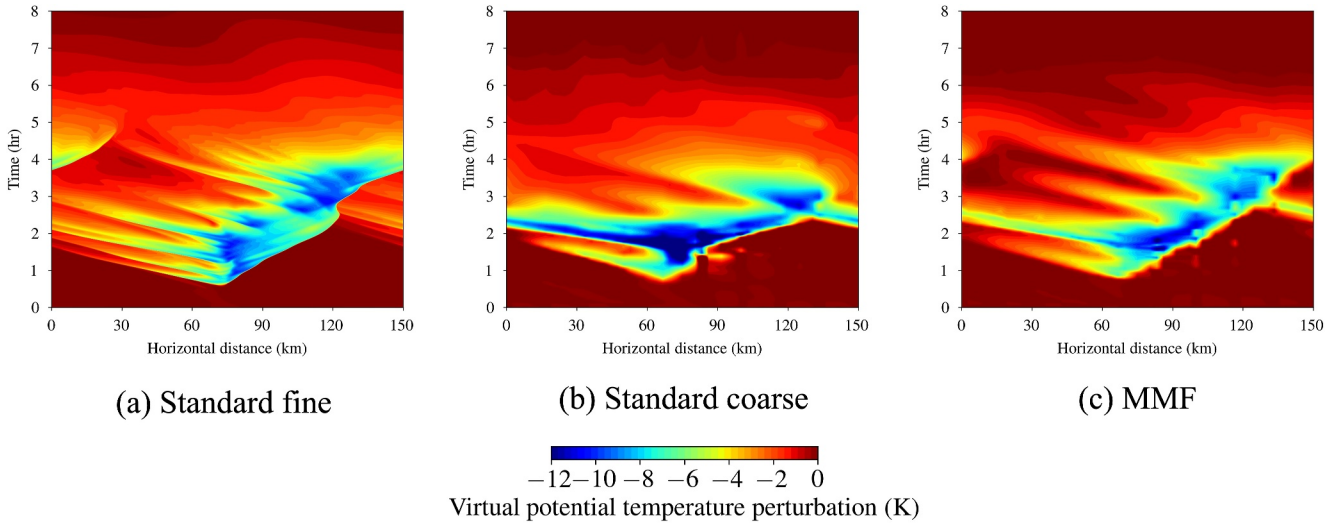

Figure 8. Contours of the VPT perturbations at the surface for the squall line, computed from the standard fine (a), standard coarse (b), and MMF (c) simulations.

Figure 10 compares the averaged profiles of the horizontal velocity and VPT perturbation along the vertical direction. These profiles are calculated by averaging in time over the whole duration and averaging along the horizontal at each height. The MMF slightly improves the results for the horizontal velocity perturbation, while underestimating the VPT in the troposphere. The reasons for this behavior would make for interesting future work.

Table 2 summarizes the wall clock time taken in the three simulations. For a comparison, the three simulations were run for a duration of 3600 s using 9 CPUs. Since the MMF simulation involves spatially and temporally refined small-scale calculations, it requires significantly more computational time, more than double that of the standard fine simulation. The total number of SSP grid points in the MMF is 2.17 times larger than the number of grid points in the fine simulation (Table 1). Therefore, the wall clock time ratio of 2.44 between the MMF and fine simulations is reasonable, considering the number of grid points and additional computational overheads.

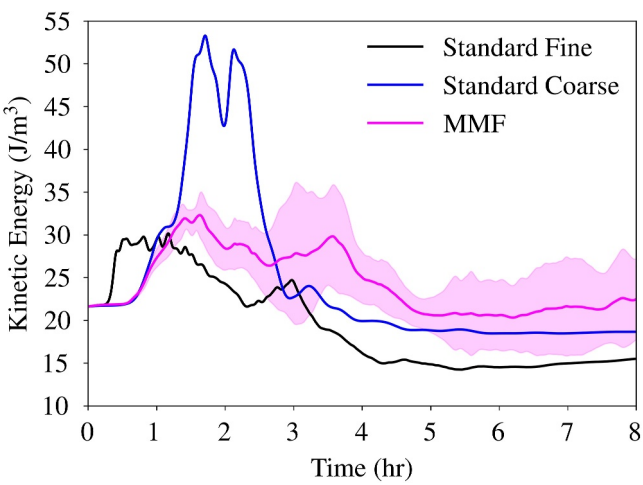

Figure 9. Averaged kinetic energy per volume versus time for the squall line. The solid pink line shows the ensemble mean kinetic energy per volume for the 20-member ensemble run of MMF, while the shaded pink area is the ensemble spread (standard deviation).

5.2. 3D Supercell

This test case is a benchmark problem that investigates the three-dimensional evolution of a supercell storm (Tissaoui et al., 2023). The dimensions of the domain are 150 and 100 km in the horizontal directions, and 24 km in height. The x axis is in the streamwise direction, the y axis is in the crosswind direction, and the z axis is in the vertical direction. The impermeable boundary condition is applied at the bottom surface, and periodic boundary conditions are applied at the lateral boundaries in both the x and y directions. At the model top, we apply the implicit sponge layer with the same thickness and coefficient values defined in Section 4.3.

The reference fields are constructed based on the atmosphere sounding provided in Tissaoui et al. (2023). For initializing the problem, a thermal perturbation defined by Equations 27 and 31 is added on top of the reference state. The radial distance in the elliptical thermal bubble is defined as

$$r = \sqrt{\left(\frac{x - x_c}{r_x}\right)^2 + \left(\frac{y - y_c}{r_y}\right)^2 + \left(\frac{z - z_c}{r_z}\right)^2}, \tag{31}$$

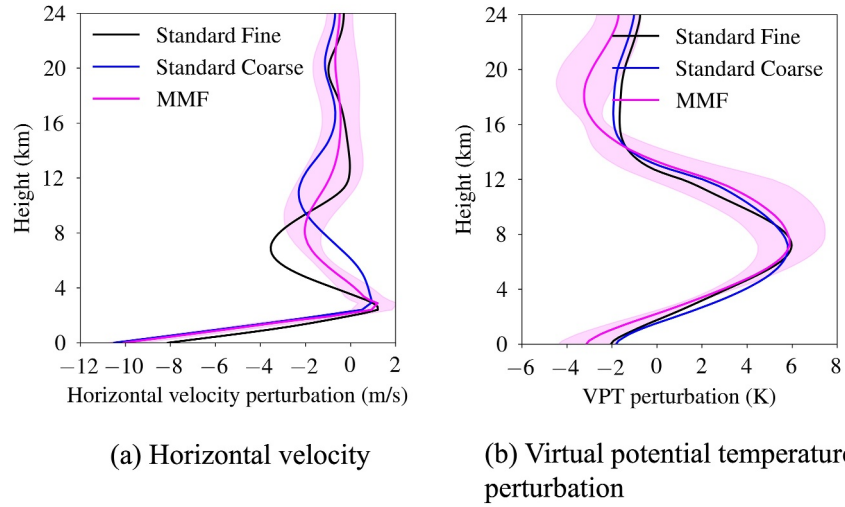

Figure 10. Averaged profiles of horizontal velocity (a) and VPT perturbation (b) with respect to height for the squall line. The solid pink line shows the ensemble mean profile for the 20-member ensemble run of MMF, while the shaded pink area is the ensemble spread (standard deviation).

where the coordinates of the center are $(x_c, y_c, z_c) = (75, 50, 2)$ km, and the semi-major axes are $r_x = r_y = 10$ km and $r_z = 2$ km, respectively. The SSP models are two-dimensional and aligned with the streamwise direction (the x-axis) of the background wind. The SSP models are initialized with the initial state values along the LSP columns. Likewise in the squall line case, we add a random perturbation to the initial VPT with an amplitude of 0.3 K, as defined in Equation 29.

We compare the standard coarse and MMF simulations with a uniform resolution of 2.5 km by 500 m along the horizontal and vertical directions, respectively. The standard fine grid simulation, with a resolution of 500 m in all directions, serves as the benchmark for this comparison. The width and height of the SSP domains in the MMF are 8 and 24 km, respectively. Table 3 summarizes the domain sizes and grid resolutions for the three simulations. The 2D SSP domains are aligned with the background wind direction. Fourth order basis functions are used in all directions. Numerical diffusion with a magnitude of $\nu = 200$ m^2/s is added to all the models. The Boyd-Vandeven filter (Boyd, 1996) with strength of 4% is applied to the standard models and the LSP model in the MMF. The semi-implicit ARK2 method (Giraldo et al., 2013) is used to integrate the equations in time until $t = 9600$ s. The time-step size is $\Delta t = 0.5$ s for the standard fine grid simulation, and $\Delta t = 2.0$ s for the standard coarse grid simulation. In the LSP model of the MMF simulation, the time-step size is $\Delta T = 2.0$ s, and each time step involves 4 sub-steps for updating the SSP variables.

The supercell cloud is initiated by a thermal perturbation and rises developing into cumulonimbus clouds, eventually merging into the wider cloud around the inversion layer. The position of the rain concentration follows the location of the convective towers, with the rain falling below the cloud towers. Figure 11 displays the instantaneous VPT field at various time steps. Since the evolution of the supercell is symmetric with respect to the

Table 2
Wall Clock Time for Squall Line Simulations With a Duration of 3600 s and Using 9 CPUs

	Standard fine	Standard coarse	MMF
Δt (sec)	0.2	2.0	2.0
Wall clock time (sec)	1,402.0	4.5	3,418.2

Table 3
Domain Size and Grid Resolution for the Supercell Simulations

			MMF	
	Standard fine	Standard coarse	LSP	SSP
Domain Size (km)	150 × 100 ×24	150 × 100 ×24	150 × 100 ×24	8 × 24
Δx (m)	500	2,500	2,500	500
Δy (m)	500	2,500	2,500	–
Δz (m)	500	500	500	500
Δt (sec)	0.5	2.0	2.0	0.5

mid x–z plane, we only show the storm patterns in one half of the domain. Like the 2D squall line test, the standard coarse grid produces more clouds than the benchmark fine grid simulation. It is conjectured that these spurious clouds in the standard coarse simulation are attributed to the large grid size that degrades the accuracy in the parametrization of the moist microphysics. The MMF simulation produces improved results in terms of the size of the clouds and the patterns of the temperature field at the surface. Even though the LSP grid of the MMF case has the same 2 km resolution, the SSP models resolve the cloud motions locally and parameterizes them according to the appropriate grid size. As a result, the quality of the solution within the LSP domain is enhanced in the MMF case.

A wider cloud pattern in the MMF simulation can be attributable to the lack of resolution in the crosswind direction. The cloud patterns in the supercell simulations turn out to be highly sensitive to the grid resolution. As we incorporated the 2D SSP grids aligned with the background wind direction, there is no control in the crosswind direction even in the MMF simulation. To investigate the role of crosswind-direction resolution, we run two additional MMF simulations by increasing resolution in the y-direction. Figure 12 demonstrates that increasing the resolution only in the y-direction reduces the cloud size and improves the MMF simulations. This confirms the critical role of the transverse resolution, motivating our future work to further develop a 3D MMF capable of providing refinement advantages in all directions.

Figure 13 displays contours of the surface precipitation patterns in x-y-t space. While the standard fine case shows a narrow spread of surface precipitation, the standard coarse case shows a wider spread in both the streamwise and crosswind directions and the rain reaches the lateral boundaries in the y direction at around $t = 9600$ s. The surface rain in the MMF simulation also reaches the lateral boundaries, but it exhibits a narrower distribution, particularly along the SSP grid direction, compared to the standard coarse case. These results verify that the MMF improves the representation of the moist microphysics and enhances accuracy in predicting surface precipitation.

Figure 14 compares the profiles of potential temperature perturbation and horizontal velocity obtained from the standard fine and coarse, and the MMF simulations. The numerical results are averaged over time and along each horizontal plane to condense them into 1D profiles. These plots show that the MMF improves (if only slightly) the results of horizontal velocity and VPT that are parameterized by the SSPs. We expect to further improve the results by simply increasing the resolution in the crosswind direction, but of course this would increase the cost of the MMF simulation.

Table 4 compares the wall clock time taken in the three simulations. For a comparison, the three simulations were run for a duration of 3,600 s using 150 CPUs. Since the MMF model is equipped with 2D SSP models and requires lower frequent MPI communications, it demands significantly less computational time compared to the standard fine simulation.

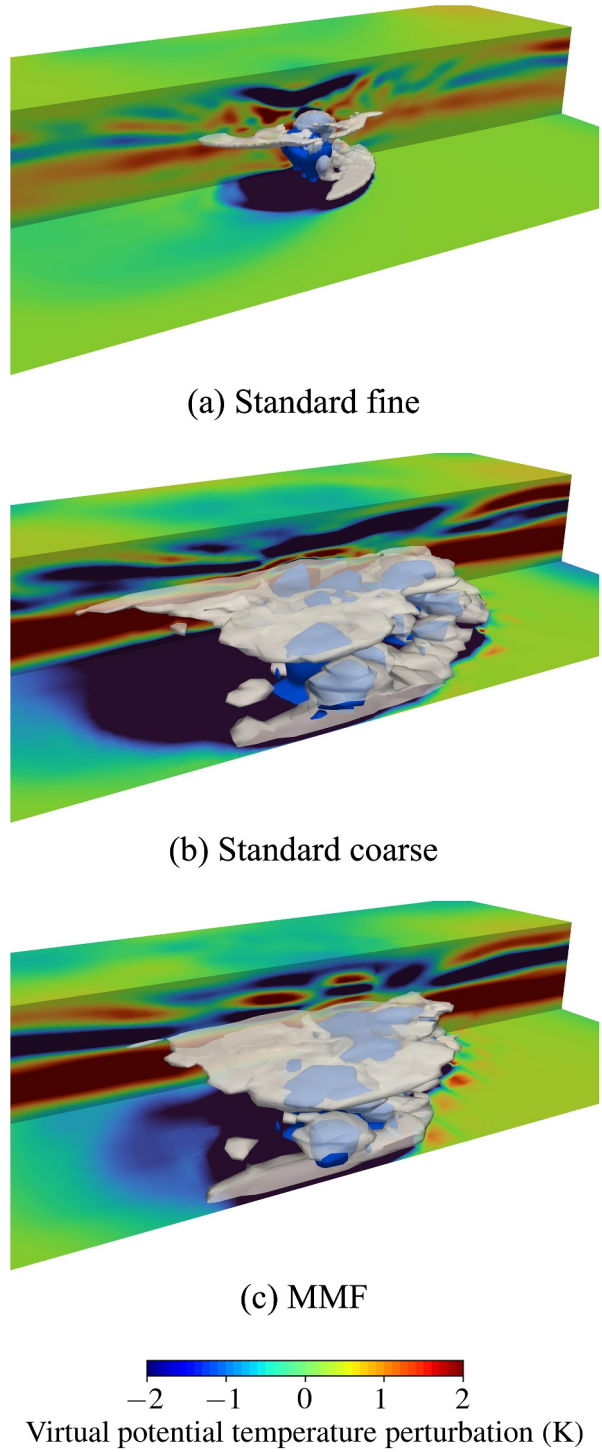

Figure 11. Instantaneous VPT perturbation field and the contours of the cloud and rain concentrations at $t = 7200$ s computed from the standard fine (a), standard coarse (b), and MMF (c) simulations for the supercell. The gray surface represents the contour of the cloud mixing ratio at $q_c = 10^{-5}$ kg/kg, and the light-blue surface represents the contours of the rain mixing ratio at $q_r = 10^{-3}$ kg/kg.

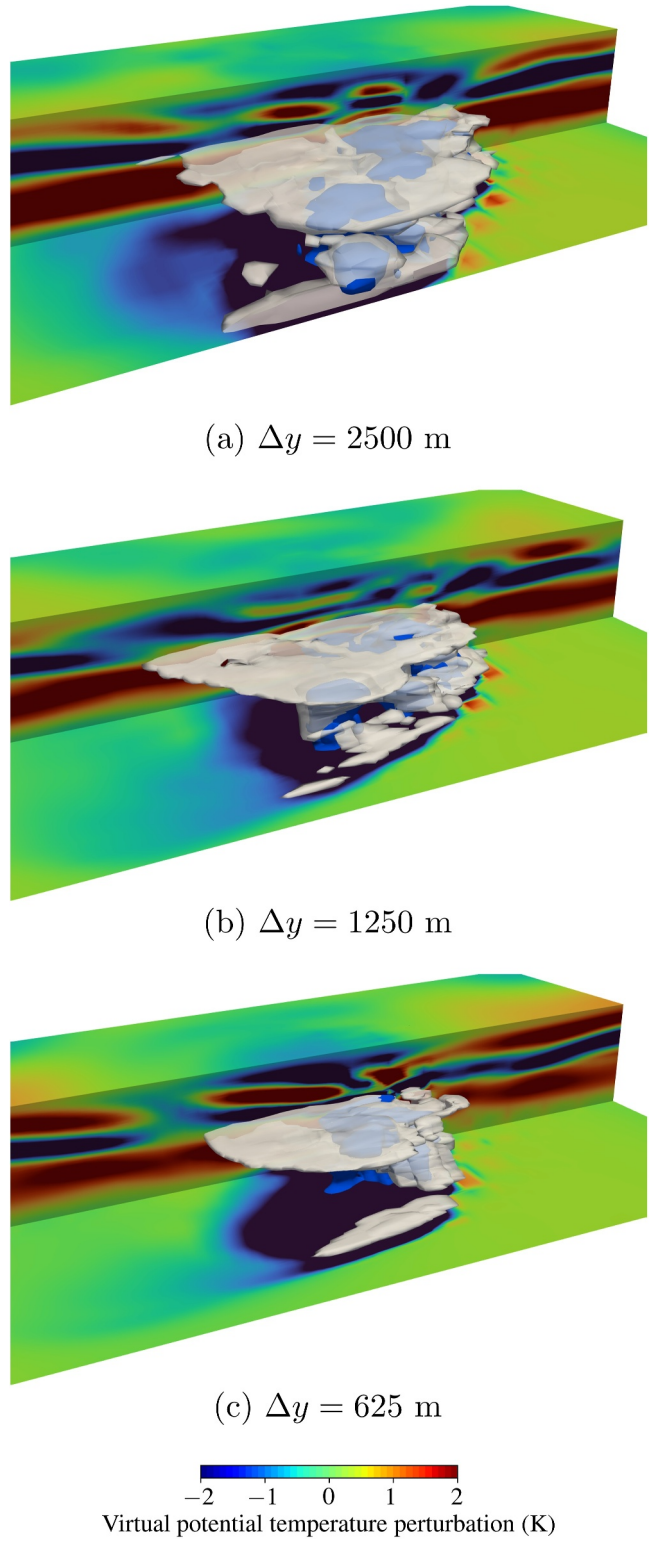

Figure 12. Instantaneous VPT perturbation field and the contours of the cloud and rain concentrations from MMF simulations of the supercell at $t = 7200$ s, using grid spacings of $\Delta y = 2500$ m (a), 1250 m (b), and 625 m (c). The gray surface represents the contour of the cloud mixing ratio at $q_c = 10^{-5}$ kg/kg, and the light-blue surface represents the contours of the rain mixing ratio at $q_r = 10^{-3}$ kg/kg.

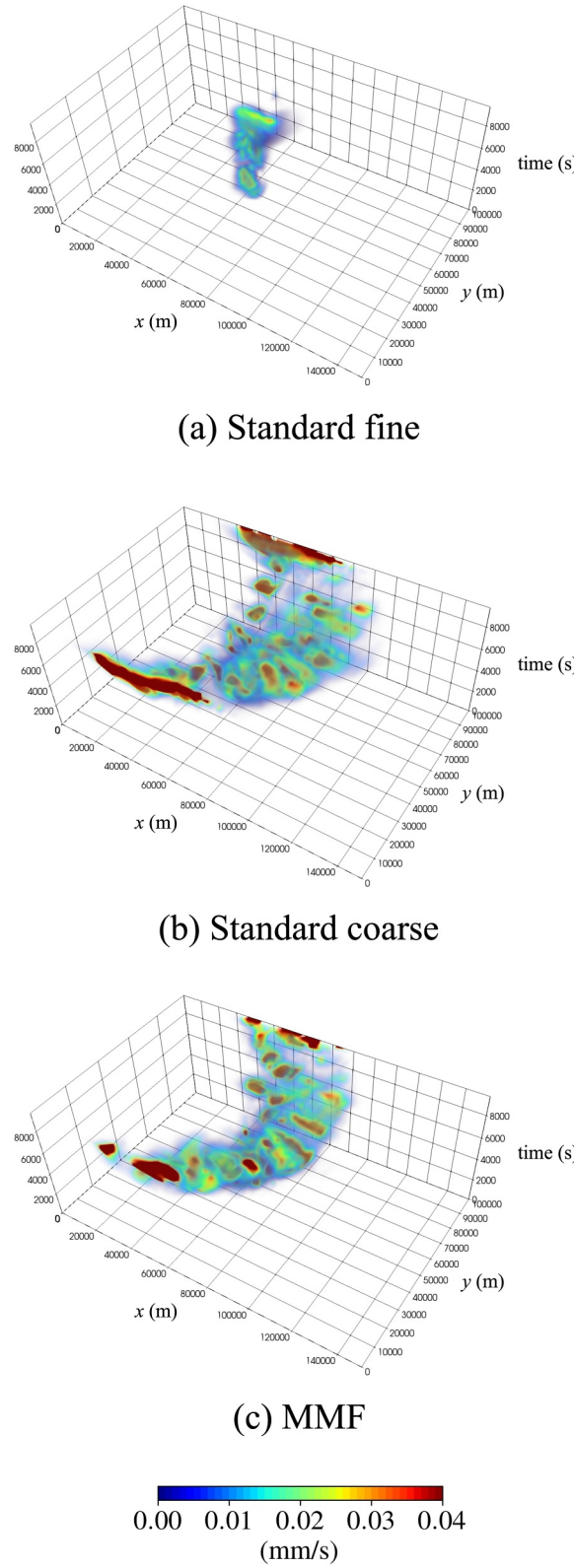

Figure 13. Volume rendering of surface precipitation for the supercell, computed from the standard fine (a), standard coarse (b), and MMF (c) simulations. The horizontal axes are the distances in the *x* and *y* directions (in meters), and the vertical axis is time (in seconds).

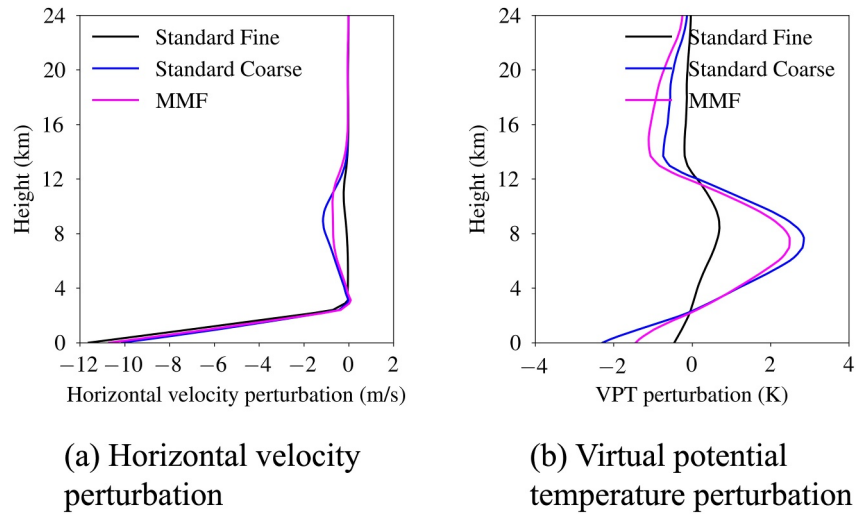

Figure 14. Averaged profiles of horizontal velocity (a) and VPT perturbation (b) with respect to height for the supercell. The results are averaged over time and the horizontal plane.

6. Conclusions

We presented a multiscale modeling framework to resolve distinct scales in large-scale and small-scale processes in the moist atmosphere. This approach aims to inject higher-dimensional feedback into a lower-dimension (coarse) model. In the MMF, we utilized the compressible Navier-Stokes equations and an element-based Galerkin method for both large-scale and small-scale models, which, to our knowledge, is the first time that a consistent approach and form of the governing equations have been used in MMF modeling. Moreover, our models are built within the same code-base. Each LSP grid column is coupled with a two dimensional SSP model, where non-conforming vertical discretization is available. This enables the adjustment of the grid spacing or the order of basis functions in the SSP model. Through a complexity analysis, we demonstrated that the MMF algorithm exhibits higher arithmetic intensity compared to the standard approach which hints at a likely better performance on exascale computing hardware.

The MMF model was tested on two weather problems: a 2D squall line and a 3D supercell storm. In the squall line test, the MMF produced improved results for instantaneous cloud patterns and the surface VPT field. This improvement was further evidenced by comparisons of the accumulated rain distribution and kinetic energy. In the supercell test, the surface rain pattern shows slight improvement along the wind direction, where the 2D SSP grids are oriented. Improvement in the crosswind direction is limited because there is no SSP refinement in this direction. Increasing the resolution in the crosswind direction enhances the MMF simulations, confirming that the limiting factor is the transverse resolution.

This research is our initial endeavor on MMF for the moist atmosphere and offers many potential avenues for extension. One such avenue is to examine ways to mitigate the cost of MMF simulations. The MMF algorithm can be optimized by simplifying SSP computations using lower-order basis functions or a fully explicit time integrator, or by reducing the number of SSPs per LSP column (Hannah et al., 2021). Developing reduced-order approximations, such as via proper orthogonal decomposition or neural networks, is a viable option to substitute the SSP models. Another avenue to explore concerns new configurations of MMF, in which 3D SSP models are coupled with each element column of the LSP model instead of the grid column for dimensional consistency. Finally, deploying the SSP simulations on GPUs can be a promising approach to accelerate time to solution for the MMF simulations.

Table 4
Wall Clock Time for Supercell Simulations With a Duration of 3600 s and Using 150 CPUs

	Standard fine	Standard coarse	MMF
Δt (sec)	0.5	2.0	2.0
Wall clock time (sec)	4,260.4	22.6	1,297.4

Appendix A: Complexity Analysis

In this section, we analyze the computational complexity of the MMF algorithm in terms of the number of floating-point operations, memory communications, and arithmetic intensity. We also compare the complexities of the standard and MMF simulations.

A1. Floating-Point Operations

We first evaluate the total number of floating-point arithmetic operations, denoted as F, throughout the duration of the simulations. The number of operations for the standard (S) and MMF (M) simulation are evaluated as

$$F^S = N_t^S N_e^S N_p^3 (816 N_p + 4635), \tag{A1a}$$

$$F^M = N_t^M N_e^M \left(1 + R_t R_x R_z N_p\right) N_p^3 (816 N_p + 4635), \tag{A1b}$$

where N_t is the number of time steps, N_e is the number of elements, and N_p is the number of nodes within an element, where the order is the same in all directions. In a single simulation, the asymptotic complexity $\mathcal{O}(N_p^4)$ arises from the gradient and divergence kernels, which constitute the dominant cost in constructing the right-hand side vector. For an MMF, R_t, R_x, and R_z represent the temporal and spatial refinement ratios between the LSP and SSP $\left(R_t, R_x, R_z \geq 1\right)$. Note that there is no refinement in the y direction, as we only employ 2D SSP models in this work.

In order to express F in terms of grid size, let us define the number of elements N_e and the number of time steps N_t for standard and MMF simulations as follows:

$$N_e^S = \frac{L_x L_y L_z}{N^3 \Delta x \Delta y \Delta z}, \qquad N_e^M = \frac{L_x L_y L_z}{N^3 R_x R_z \Delta x \Delta y \Delta z}, \tag{A2}$$

where L_x, L_y, and L_z are the lengths of the domain in the x, y, z directions, respectively. The grid sizes Δx, Δy, and Δz for the standard simulation are set equal to the grid size of the SSP in the MMF simulation. The number of time steps for the time duration T are counted as

$$N_t^S = \frac{T}{\Delta t}, \qquad N_t^M = \frac{T}{R_t \Delta t}, \tag{A3}$$

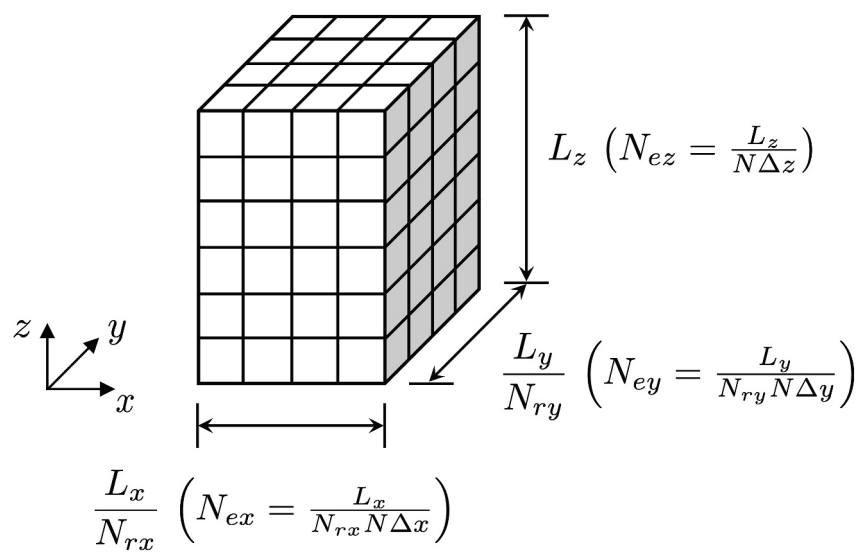

Figure A1. Dimensions of a grid partition assigned to an MPI rank and the number of elements along each direction. (N_{ex}, N_{ey}, and N_{ez} are the number of elements along the x, y, z directions).

where the same time step size Δt is assumed for the standard and the SSP of MMF simulations.

Substituting Equations A2 and A3 into Equation A1, we obtain the following expressions for the number of floating-point (F) operations:

$$F^S = \left(\frac{T}{\Delta t}\right)\left(\frac{L_x L_y L_z}{N^3 \Delta x \Delta y \Delta z}\right) N_p^3 (816 N_p + 4635), \tag{A4a}$$

$$F^M = \left(\frac{T}{\Delta t}\right)\left(\frac{L_x L_y L_z}{N^3 \Delta x \Delta y \Delta z}\right)\left(\frac{1}{R_t R_x R_z} + N_p\right) N_p^3 (816 N_p + 4635). \tag{A4b}$$

It can be seen that the MMF simulation requires more floating-point operations than the standard simulation by a factor of $\left(1/\left(R_t R_x R_z\right) + N_p\right)$.

A2. Communication

In this analysis, we only consider communications among MPI processes in the distributed-memory system for comparisons. The transfer of shared data within cores is neglected. The data transfer occurs at the points on the lateral boundaries of the grid partitions in Figure 4. The total amount of floating-point numerical data to transfer or bytes (B) is evaluated as follows:

$$B^S = N_t^S N_r \left(784 N_{p,\Gamma}^S\right), \tag{A5a}$$

$$B^M = N_t^M N_r \left(784 N_{p,\Gamma}^M\right), \tag{A5b}$$

where N_r is the number of ranks (the same for the standard and the MMF) and we assume the use of double precision so that each floating-point number occupies 8 bytes. The number of points at the lateral boundaries of the grid partition $N_{p,\Gamma}$ within a rank is

$$N_{p,\Gamma}^S = 2\left(\frac{L_x}{N_{rx} N \Delta x} + \frac{L_y}{N_{ry} N \Delta y}\right)\left(\frac{L_z}{N \Delta z}\right) N_p^2, \tag{A6a}$$

$$N_{p,\Gamma}^M = 2\left(\frac{L_x}{R_x N_{rx} N \Delta x} + \frac{L_y}{N_{ry} N \Delta y}\right)\left(\frac{L_z}{R_z N \Delta z}\right) N_p^2, \tag{A6b}$$

where N_{rx} and N_{ry} are the number of ranks in the x and y directions ($N_r = N_{rx} \times N_{ry}$), respectively. Figure A1 shows the number of elements along each direction at the communicating boundaries. Since inter-process communications occur only in the LSP model for MMF, there are fewer communicating points and, consequently, less data movement in the MMF. Substituting Equations A3 and A6 into Equation A5, we obtain

$$B^S = 1568 N_r \left(\frac{T}{\Delta t}\right)\left(\frac{L_x}{N_{rx} N \Delta x} + \frac{L_y}{N_{ry} N \Delta y}\right)\left(\frac{L_z}{N \Delta z}\right) N_p^2, \tag{A7a}$$

$$B^M = \frac{1568 N_r}{R_t R_z}\left(\frac{T}{\Delta t}\right)\left(\frac{L_x}{R_x N_{rx} N \Delta x} + \frac{L_y}{N_{ry} N \Delta y}\right)\left(\frac{L_z}{N \Delta z}\right) N_p^2. \tag{A7b}$$

A3. Arithmetic Intensity

Arithmetic intensity I is the ratio of total floating-point (F) operations to total data movement/bytes (B), calculated as $I = F/B$. For simplicity, we assume the following: $N_{rx} = N_{ry} = N_r$, $L_x = L_y = L$, $\Delta x = \Delta y$, $R_x = R_t = R$ and $R_z = 1$. Consequently, the arithmetic intensity for the standard and MMF simulations is calculated using Equations A4 and A7 as

$$I^S = \frac{F^S}{B^S} = \frac{1}{2\left(\frac{N_r N \Delta x}{L}\right)} N_p (0.520 N_p + 2.956), \tag{A8a}$$

$$I^M = \frac{F^M}{B^M} = \frac{\left(\frac{1}{R} + R N_p\right)}{\left(\frac{1}{R} + 1\right)\left(\frac{N_r N \Delta x}{L}\right)} N_p (0.520 N_p + 2.956). \tag{A8b}$$

Equation A8 illustrates that the arithmetic intensity for MMF is much higher than that of the standard simulation, that is, $I^M > I^S$:

$$\frac{I^M}{I^S} = \frac{2\left(\frac{1}{R} + R N_p\right)}{\left(\frac{1}{R} + 1\right)} \tag{A9}$$

because $\frac{I^M}{I^S} > 1$ when $R > 1$. This suggests that the MMF algorithm has the potential to overcome the memory-bound limitations that large-scale simulations typically encounter.

Data Availability Statement

Figures of instantaneous fields in the squall line test were made using Matlab (The MathWorks Inc., 2022). Figures of instantaneous fields in the supercell test were made using Paraview (Ayachit, 2015). Other figures were produced using Matplotlib (Hunter, 2007). The figures and data for squall line and supercell simulations associated with this manuscript are available on Zenodo repository (Kang, 2024).

Acknowledgments
This work was supported by the Office of Naval Research under Grant N0001419WX00721. F. X. Giraldo was also supported by the National Science Foundation under Grant AGS-1835881. This work was performed when Soonpil Kang held a National Academy of Sciences' National Research Council Fellowship at the Naval Postgraduate School. Part of Soonpil Kang's work was performed under the auspices of the U.S. Department of Energy by Lawrence Livermore National Laboratory under Contract DE-AC52-07NA27344. LLNL-JRNL-2005873. We would like to thank Wojciech W. Grabowski (National Center for Atmospheric Research) and Walter Hannah (Lawrence Livermore National Laboratory) for their helpful discussions. We also thank Wojciech W. Grabowski and the other reviewer for their constructive feedback, which helped improve the manuscript.

References

Arakawa, A., & Konor, C. S. (2009). Unification of the Anelastic and quasi-hydrostatic systems of equations. *Monthly Weather Review*, *137*(2), 710–726. https://doi.org/10.1175/2008mwr2520.1

Ayachit, U. (2015). The paraview guide: A parallel visualization application [Software]. *Clifton Park, NY, USA: Kitware, Inc*. https://doi.org/10.5555/2789330

Boyd, J. P. (1996). The ERFC-log filter and the asymptotics of the Euler and Vandeven sequence accelerations. In *Proceedings of the third International Conference on spectral and high order methods* (pp. 267–276).

Bryan, G. H., & Fritsch, J. M. (2002). A benchmark simulation for moist nonhydrostatic numerical models. *Monthly Weather Review*, *130*(12), 2917–2928. https://doi.org/10.1175/1520-0493(2002)130<2917:absfmn>2.0.co;2

Eckermann, S. D., Barton, C. A., & Kelly, J. F. (2023). Adaptation of θ-based dynamical cores for extension into the thermosphere using a hybrid virtual potential temperature. *Monthly Weather Review*, *151*(8), 1937–1955. https://doi.org/10.1175/mwr-d-22-0320.1

Gaberšek, S., Giraldo, F. X., & Doyle, J. D. (2012). Dry and moist idealized experiments with a two-dimensional spectral element model. *Monthly Weather Review*, *140*(10), 3163–3182. https://doi.org/10.1175/mwr-d-11-00144.1

Giraldo, F. X. (1998). The Lagrange–Galerkin spectral element method on unstructured quadrilateral grids. *Journal of Computational Physics*, *147*(1), 114–146. https://doi.org/10.1006/jcph.1998.6078

Giraldo, F. X. (2020). *An introduction to element-based Galerkin methods on tensor-product bases: Analysis, algorithms, and applications* (Vol. 24). Springer International Publishing. https://doi.org/10.1007/978-3-030-55069-1

Giraldo, F. X., de Bragança Alves, F. A., Kelly, J. F., Kang, S., & Reinecke, P. A. (2024). A performance study of Horizontally Explicit Vertically Implicit (HEVI) time-integrators for non-hydrostatic atmospheric models. *Journal of Computational Physics*, *515*, 113275. https://doi.org/10.1016/j.jcp.2024.113275

Giraldo, F. X., Kelly, J. F., & Constantinescu, E. M. (2013). Implicit-explicit formulations of a three-dimensional Nonhydrostatic Unified Model of the Atmosphere (NUMA). *SIAM Journal on Scientific Computing*, *35*(5), B1162–B1194. https://doi.org/10.1137/120876034

Grabowski, W. W. (2001). Coupling cloud processes with the large-scale dynamics using the Cloud-Resolving Convection Parameterization (CRCP). *Journal of the Atmospheric Sciences*, *58*(9), 978–997. https://doi.org/10.1175/1520-0469(2001)058<0978:ccpwtl>2.0.co;2

Grabowski, W. W. (2004). An improved framework for superparameterization. *Journal of the Atmospheric Sciences*, *61*(15), 1940–1952. https://doi.org/10.1175/1520-0469(2004)061<1940:aiffs>2.0.co;2

Grabowski, W. W. (2016). Towards global large eddy simulation: Super-parameterization revisited. *Journal of the Meteorological Society of Japan. Ser. II*, *94*(4), 327–344. https://doi.org/10.2151/jmsj.2016-017

Grabowski, W. W., & Smolarkiewicz, P. K. (1999). CRCP: A cloud resolving convection parameterization for modeling the tropical convecting atmosphere. *Physica D: Nonlinear Phenomena*, *133*(1–4), 171–178. https://doi.org/10.1016/s0167-2789(99)00104-9

Han, Y., Zhang, G. J., Huang, X., & Wang, Y. (2020). A moist physics parameterization based on deep learning. *Journal of Advances in Modeling Earth Systems*, *12*(9), e2020MS002076. https://doi.org/10.1029/2020ms002076

Hannah, W. M., Bradley, A. M., Guba, O., Tang, Q., Golaz, J.-C., & Wolfe, J. (2021). Separating physics and dynamics grids for improved computational efficiency in spectral element earth system models. *Journal of Advances in Modeling Earth Systems*, *13*(7), e2020MS002419. https://doi.org/10.1029/2020ms002419

Hannah, W. M., Jones, C. R., Hillman, B. R., Norman, M. R., Bader, D. C., Taylor, M. A., et al. (2020). Initial results from the super-parameterized E3SM. *Journal of Advances in Modeling Earth Systems*, *12*(1), e2019MS001863. https://doi.org/10.1029/2019ms001863

Hogan, T. F., Liu, M., Ridout, J. A., Peng, M. S., Whitcomb, T. R., Ruston, B. C., et al. (2014). The Navy global environmental model. *Oceanography*, *27*(3), 116–125. https://doi.org/10.5670/oceanog.2014.73

Hogan, T. F., & Rosmond, T. E. (1991). The description of the Navy operational global atmospheric prediction system's spectral forecast model. *Monthly Weather Review*, *119*, 1786–1815. https://doi.org/10.1175/1520-0493(1991)119⟨1786:TDOTNO⟩2.0.CO;2

Hunter, J. D. (2007). Matplotlib: A 2D graphics environment [Software]. *Computing in Science & Engineering*, *9*(3), 90–95. https://doi.org/10.1109/MCSE.2007.55

Jansson, F., van den Oord, G., Pelupessy, I., Grönqvist, J. H., Siebesma, A. P., & Crommelin, D. (2019). Regional superparameterization in a global circulation model using large eddy simulations. *Journal of Advances in Modeling Earth Systems*, *11*(9), 2958–2979. https://doi.org/10.1029/2018ms001600

Jung, J.-H., & Arakawa, A. (2010). Development of a quasi-3D multiscale modeling framework: Motivation, basic algorithm and preliminary results. *Journal of Advances in Modeling Earth Systems*, *2*(4). https://doi.org/10.3894/james.2010.2.11

Kang, S. (2024). MMF for moist atmosphere [Dataset]. *Zenodo*. https://doi.org/10.5281/zenodo.11166368

Kelly, J. F., & Giraldo, F. X. (2012). Continuous and discontinuous Galerkin methods for a scalable three-dimensional nonhydrostatic atmospheric model: Limited-area mode. *Journal of Computational Physics*, *231*(24), 7988–8008. https://doi.org/10.1016/j.jcp.2012.04.042

Khairoutdinov, M., Randall, D., & DeMott, C. (2005). Simulations of the atmospheric general circulation using a cloud-resolving model as a superparameterization of physical processes. *Journal of the Atmospheric Sciences*, *62*(7), 2136–2154. https://doi.org/10.1175/jas3453.1

Khairoutdinov, M. F., & Randall, D. A. (2001). A cloud resolving model as a cloud parameterization in the NCAR community climate system model: Preliminary results. *Geophysical Research Letters*, *28*(18), 3617–3620. https://doi.org/10.1029/2001gl013552

Khairoutdinov, M. F., & Randall, D. A. (2003). Cloud resolving modeling of the ARM summer 1997 IOP: Model formulation, results, uncertainties, and sensitivities. *Journal of the Atmospheric Sciences*, *60*(4), 607–625. https://doi.org/10.1175/1520-0469(2003)060<0607:crmota>2.0.co;2

Klemp, J. B., Dudhia, J., & Hassiotis, A. (2008). An upper gravity-wave absorbing layer for NWP applications. *Monthly Weather Review*, *136*(10), 3987–4004. https://doi.org/10.1175/2008mwr2596.1

Klemp, J. B., & Wilhelmson, R. B. (1978). The simulation of three-dimensional convective storm dynamics. *Journal of the Atmospheric Sciences*, *35*(6), 1070–1096. https://doi.org/10.1175/1520-0469(1978)035<1070:tsotdc>2.0.co;2

Kooperman, G. J., Pritchard, M. S., Burt, M. A., Branson, M. D., & Randall, D. A. (2016). Robust effects of cloud superparameterization on simulated daily rainfall intensity statistics across multiple versions of the Community Earth System Model. *Journal of Advances in Modeling Earth Systems*, *8*(1), 140–165. https://doi.org/10.1002/2015ms000574

Kopera, M. A., & Giraldo, F. X. (2014). Analysis of adaptive mesh refinement for IMEX discontinuous Galerkin solutions of the compressible Euler equations with application to atmospheric simulations. *Journal of Computational Physics*, *275*, 92–117. https://doi.org/10.1016/j.jcp.2014.06.026

Kopera, M. A., & Giraldo, F. X. (2015). Mass conservation of the unified continuous and discontinuous element-based Galerkin methods on dynamically adaptive grids with application to atmospheric simulations. *Journal of Computational Physics*, *297*, 90–103. https://doi.org/10.1016/j.jcp.2015.05.010

Kopriva, D. A. (1996). A conservative staggered-grid Chebyshev multidomain method for compressible flows. II: A semi-stuctured method. *Journal of Computational Physics*, *128*(2), 475–488. https://doi.org/10.1006/jcph.1996.0225

Kopriva, D. A. (2009). *Implementing spectral methods for partial differential equations: Algorithms for scientists and engineers*. Springer Science & Business Media.

Kurowski, M. J., Grabowski, W. W., & Smolarkiewicz, P. K. (2015). Anelastic and compressible simulation of moist dynamics at planetary scales. *Journal of the Atmospheric Sciences*, *72*(10), 3975–3995. https://doi.org/10.1175/jas-d-15-0107.1

Lin, G., Jones, C. R., Leung, L. R., Feng, Z., & Ovchinnikov, M. (2022). Mesoscale convective systems in a superparameterized E3SM simulation at high resolution. *Journal of Advances in Modeling Earth Systems*, *14*(1), e2021MS002660. https://doi.org/10.1029/2021ms002660

Lin, G., Leung, L. R., Lee, J., Harrop, B. E., Baker, I. T., Branson, M. D., et al. (2023). Modeling land-atmosphere coupling at cloud-resolving scale within the Multiple Atmosphere Multiple Land (MAML) framework in SP-E3SM. *Journal of Advances in Modeling Earth Systems*, *15*(2), e2022MS003101. https://doi.org/10.1029/2022ms003101

Majda, A. J., & Grooms, I. (2014). New perspectives on superparameterization for geophysical turbulence. *Journal of Computational Physics*, *271*, 60–77. https://doi.org/10.1016/j.jcp.2013.09.014

Majda, A. J., & Xing, Y. (2010). New multi-scale models on mesoscales and squall lines. *Communications in Mathematical Sciences*, *8*(1), 113–134. https://doi.org/10.4310/cms.2010.v8.n1.a7

Marras, S., Kelly, J. F., Moragues, M., Müller, A., Kopera, M. A., Vázquez, M., et al. (2016). A review of element-based Galerkin methods for numerical weather prediction: Finite elements, spectral elements, and discontinuous Galerkin. *Archives of Computational Methods in Engineering*, *23*(4), 673–722. https://doi.org/10.1007/s11831-015-9152-1

Pritchard, M. S., & Somerville, R. C. (2009). Empirical orthogonal function analysis of the diurnal cycle of precipitation in a multi-scale climate model. *Geophysical Research Letters*, *36*(5). https://doi.org/10.1029/2008gl036964

Randall, D., Khairoutdinov, M., Arakawa, A., & Grabowski, W. (2003). Breaking the cloud parameterization deadlock. *Bulletin of the American Meteorological Society*, *84*(11), 1547–1564. https://doi.org/10.1175/bams-84-11-1547

Rotunno, R., Klemp, J. B., & Weisman, M. L. (1988). A theory for strong, long-lived squall lines. *Journal of the Atmospheric Sciences*, *45*(3), 463–485. https://doi.org/10.1175/1520-0469(1988)045<0463:atfsll>2.0.co;2

Saad, Y., & Schultz, M. H. (1986). GMRES: A generalized minimal residual algorithm for solving nonsymmetric linear systems. *SIAM Journal on Scientific and Statistical Computing*, *7*(3), 856–869. https://doi.org/10.1137/0907058

The MathWorks Inc. (2022). Matlab version: 9.13.0 (r2022b) [Software]. https://www.mathworks.com

Tissaoui, Y., Marras, S., Quaini, A., de Brangaca Alves, F. A., & Giraldo, F. X. (2023). A non-column based, fully unstructured implementation of Kessler's microphysics with warm rain using continuous and discontinuous spectral elements. *Journal of Advances in Modeling Earth Systems*, *15*(3), e2022MS003283. https://doi.org/10.1029/2022ms003283

Vallis, G. K. (2005). *Atmospheric and oceanic fluid dynamics*. Cambridge University Press.

Xing, Y., Majda, A. J., & Grabowski, W. W. (2009). New efficient sparse space–time algorithms for superparameterization on mesoscales. *Monthly Weather Review*, *137*(12), 4307–4324. https://doi.org/10.1175/2009mwr2858.1

Yi, T.-H., & Giraldo, F. X. (2020). Vertical discretization for a nonhydrostatic atmospheric model based on high-order spectral elements. *Monthly Weather Review*, *148*(1), 415–436. https://doi.org/10.1175/mwr-d-18-0283.1

Zaron, E. D., Chua, B. S., Reinecke, P. A., Michalakes, J., Doyle, J. D., & Xu, L. (2022). The tangent-linear and adjoint models of the NEPTUNE dynamical core. *Tellus A: Dynamic Meteorology and Oceanography*, *74*(1), 399–411. https://doi.org/10.16993/tellusa.146